Mechanical Systems and Signal Processing 237 (2025) 112972

Contents lists available at ScienceDirect

Mechanical Systems and Signal Processing

journal homepage: www.elsevier.com/locate/ymssp

Full Length Article

Fundamental frequency optimization of variable stiffness Multi-Region composite panels in Presence of geometrical nonlinearity☆

Touraj Farsadi [a], Majid Ahmadi [a], Shakir Jiffri [b,*], Hamed Haddad Khodaparast [b], Hasan Kurtaran [a], Michael I. Friswell [b], Sebastiano Fichera [c]

[a] Adana Alparslan Turkes Science and Technology University, Aerospace Engineering Department, Türkiye
[b] Swansea University, Faculty of Science and Engineering, UK
[c] University of Liverpool, Mechanical and Aerospace Engineering Department, UK

ARTICLE INFO

Keywords:
Curvilinear Fiber Paths
Composite panels
Vibration
Optimisation
Geometrical Nonlinearity

ABSTRACT

Multi-region laminate optimization offers a comprehensive approach to enhance aerospace structures, making them efficient, safe, and cost-effective. Similarly, Automated Fiber Placement (AFP) processes optimize toolpaths and fiber deposition, reducing waste, saving time, and improving composite quality. Strategically placing fibers where needed, it boosts structural performance and allows for innovative composite designs. This study, first, focuses on optimizing the Fundamental Natural Frequency (FNF) of composite panels, which feature various Curvilinear Fiber Paths (CFP) mathematically modeled using bilinear interpolation distributed across different regions of the panel with comparisons drawn against the conventional Unidirectional (UD) fiber layup. Secondly, a study is conducted to explore the Fundamental Amplitude-dependent Nonlinear Frequencies (FANF) within the context of the optimized configuration featuring curved fiber layup. The modulation of stiffness in composite laminates is achieved through continuous adjustments of fiber angles, governed by the CFP function. A nonlinear structural model, grounded in the principles of virtual work, is employed for this analysis. The formulation incorporates Green's nonlinear kinematic strain relations to accommodate geometric nonlinearities, and First-order Shear Deformation Theory (FSDT) is applied to extend the analysis to moderately thick cylindrical panels, including transverse shear deformations. The principal aim of this investigation is to evaluate the impact of Variable Stiffness (VS) parameters across multiple regions on the linear and nonlinear free vibration characteristics of the panel. This research examines symmetric eight-layered composite panel incorporating three distinct design regions and two boundary condition sets. The Generalized Differential Quadrature (GDQ) method is employed to solve the nonlinear equations of motion governing these structures. The numerical findings show the impact of fiber angle paths and boundary conditions on the FNF of cylindrical panels.

☆ This article is part of a special issue entitled: 'Prof. Mottershead' published in Mechanical Systems and Signal Processing.

* Corresponding author.
E-mail address: shakir.jiffri@swansea.ac.uk (S. Jiffri).

https://doi.org/10.1016/j.ymssp.2025.112972
Received 15 January 2025; Received in revised form 25 April 2025; Accepted 6 June 2025
Available online 14 June 2025

1. Introduction

Manufacturing methods significantly impact aerospace structural design and the final product's quality. Recent developments in the Variable Stiffness Composite (VSC) concept have potential to maximize the benefits of composite designs. These advancements allow for more tailored and efficient wings, enhancing the overall performance and safety of flying vehicles.

The Variable Stiffness (VS) composite concept is also known as the Variable Stiffness Laminate (VSL) or Variable Angle Tow (VAT) in the literature with slight differences in interpretation. The method is capable of tailoring the stress distribution, so that the buckling/fluttering load bearing capacity is improved and more tuned vibration response characteristics are attained for any specific aerospace product, including wings and fuselages. During the late 1980 s with the introduction of Automated Fiber Placement (AFP) methods, manufacturing of almost all geometries became possible. AFP can place prepreg tapes on the mandrel/tool with much smaller tow widths and precision. During the manufacturing process, in order to minimize the voids and defects, heat and pressure are controlled precisely. New machines can control more than thirty tows, with individual controls, to be placed on the surface. Moreover, tows can be added or dropped at any point along the path of the machine head.

Continuous Stiffness Modeling (CSM) or Functional Fiber Path (FFP) representation, was first introduced by Olmedo and Gürdal [1] to perform the buckling analysis of plates with variable stiffness. Their fiber angle function definition showed an improvement of the buckling load of about 80 % with respect to the best straight fiber design. A more generalized function was then proposed by Tatting and Gürdal [2] where the fiber orientation function varies linearly along an arbitrarily defined axis upon definition of two orientation values at the beginning and end of the characteristic length, respectively. Recently, Farsadi et al. [3–5] studied VSC plates using a shear deformable theory for vibration characterization. Their results show the possibility of altering the vibration frequencies significantly in a desired way.

Optimizing aerospace structures by selecting various regions in wings and fuselages components, can significantly enhance the overall performance and efficiency of air vehicles and missiles [6,7]. Recent studies have explored innovative approaches to concurrently optimize fiber orientations across multiple scales. The work by Duan et al. [8] presents a robust multiscale framework that integrates microstructural design with global structural objectives. Similarly, da Silva et al. [9] advance the field by addressing fiber orientation optimization under stress constraints, employing a penalization strategy to achieve structurally efficient designs. These contributions highlight the growing integration of advanced mathematical schemes and manufacturing considerations in CFP optimization, complementing the methodology presented in this study.

This multi-disciplinary approach, known as Multi-Region Optimization (MRO), acknowledges that different parts of an air vehicle have unique design requirements, loading conditions, and constraints. By tailoring the design to each region, engineers can achieve weight reduction, improved structural stiffness, and enhanced dynamic performance. This strategy allows for informed trade-offs and compromises, ensures robustness in the face of uncertainties, and can lead to cost savings through more efficient material usage and manufacturing processes. It involves the utilization of advanced modeling, simulation, and optimization techniques, including finite element analysis, to achieve the best possible results. The approach of MRO is a sophisticated and computationally intensive process that offers a holistic way to improve aerospace structures, taking into account the diverse needs and challenges posed by different regions. By doing so, it ultimately results in more efficient, safer, and cost-effective air vehicles, contributing to advancements in the field of aerospace engineering. MRO can enhance the efficiency of AFP processes by optimizing the toolpaths and the deposition of fibers. Adapting the placement strategy to the specific requirements of each region, you can minimize waste, reduce manufacturing time, and improve the overall quality of the composite structure.

MRO can provide designers with greater flexibility to explore innovative and unconventional composite layouts, pushing the boundaries of what's achievable in terms of performance and weight reduction. However, it's important to note that implementing MRO in AFP processes can be challenging. It requires advanced software tools, robust modeling and simulation capabilities, and a deep understanding of material properties and manufacturing processes. Additionally, it may introduce complexities in the programming and control of the AFP machine to execute optimized toolpaths accurately.

In terms of mathematical modeling and solution approaches in FFP method, a vast variety of methods and solution algorithms are adopted. A great review is published by Ribeiro et al. [10] to show the vibrational potentials of VSC structures and the necessity of optimization for an efficient design. In what follows, some of the related studies on plate and beam structures are reviewed. Such plate models can be representative of wing and fuselage skin structures in special boundary and operating conditions. A comprehensive assessment of VSC plates is reported by Venkatachari et al. [11] using a higher order theory and the finite element method. Their findings confirm the significant effect of fiber orientation and lay-up configuration on bending deformation and vibration modes. Akhavan and Ribeiro [12,13] studied VSC plates using a shear deformable theory for vibration characterization. Their results show the possibility of altering the vibration frequencies significantly in a desired way. Flutter behavior of VSC plates using an isogeometric based optimization technique is conducted by Fazilati and Khalafi [14]. Their results also confirm the studies and shows the profound effect of fiber angle function on the flutter characteristics [15]. Daraei et al. [16] performed a free vibration analysis of VSC beams through the Carrera unified formulation along with refined theory assumptions. Kheladi et al. [17] considered the problem of VSC beams with parabolic curvilinear fibers in an equivalent single layer theory context and isogeometric analysis. Yan et al. [18] used a hierarchical differential quadrature method coupled with the quasi-three-dimensional formulation to investigate VSC beams. Patni et al. [19] used a combination of layer-wise/equivalent single layer theory and the Lagrange finite element to perform the 3D stress analysis of VSC beams. Vescovini et al. [20] presented a post-buckling analysis within a perturbation approach framework for VSC plates. Hao et al. [21] performed a structural stability analysis of VSC plates using isogeometric analysis. They included different fiber path functions, ply numbers, geometric parameters, as well as various boundary and loading conditions for the assessment of their proposed stability approach. Their method provides adequate accuracy with less computational costs. An approximate variable

kinematics approach is presented by Vescovini and Dozio [22] for stability and free vibration of VSC panels. González and Vescovini [23] presented a nonlinear vibration formulation for VSC plates using a third order shear deformation theory. The final equations are discretized by the Ritz, and Differential Quadrature (DQ)/Harmonic Balance (HB) methods. Their prominent contribution is the enhanced computational efficiency which is a key factor in optimization problems of VSC structures. Farsadi et al. [24] and Rahmanian et al. [25] presented some of the pioneering studies for nonlinear analysis of VSC plate structures.

Fundamental Amplitude-dependent Nonlinear Frequencies (FANF) refer to the variation of a structure's FNF with increasing vibration amplitude, typically observed in systems exhibiting geometric or material nonlinearity. Unlike linear systems where natural frequencies remain constant regardless of amplitude, nonlinear systems—such as variable stiffness composite panels—often show amplitude-dependent behavior, commonly referred to as softening (frequency decreases with amplitude) or hardening (frequency increases). Recent studies have emphasized the importance of nonlinear effects in the dynamic analysis of composite structures. Song et al. [26] investigated the vibration behavior of laminated conical shells under hygrothermal conditions, highlighting environmental influences. Farokhi et al. [27] developed and experimentally validated a nonlinear joint model for curved panels experiencing large-amplitude vibrations. These works support the relevance of incorporating nonlinear behavior in the vibration analysis used in this study.

Despite the significant progress in the modeling and optimization of VSC and their demonstrated benefits in structural performance, much of the existing work has focused on flat plate and beam geometries under simplified conditions. Studies addressing curved aerospace structures such as cylindrical panels, particularly in the context of both linear and amplitude-dependent nonlinear vibration characteristics, remain limited. Furthermore, while the use of continuous fiber path modeling and advanced optimization techniques has gained traction, there is a lack of comprehensive investigations combining multi-region curvilinear fiber path design with nonlinear dynamic analysis. This gap is especially evident in the context of optimizing both FNF and FANF, where interactions between geometric curvature, fiber orientation, and nonlinear stiffness effects are not yet fully understood.

This study explores the optimization of the FNF and the study of FANF of composite cylindrical panels featuring Curvilinear Fiber Paths (CFP). The CFPs are modeled using bilinear mapping across multiple regions, allowing for continuous modulation of stiffness through adjustable fiber angles. By employing the Generalized Differential Quadrature (GDQ) method and leveraging the Genetic Algorithm (GA) for optimization, this research evaluates the influence of VS parameters on both linear and nonlinear vibration characteristics. The findings provide valuable insights into the effects of fiber path configurations and boundary conditions on the dynamic behavior of composite panels.

2. Methodology

2.1. Variable stiffness description and the optimization strategy

In the context of AFP techniques, bilinear interpolation enhances precision and efficiency. It provides clear, mathematically defined paths for AFP machines to follow, ensuring accurate fiber placement and reducing material waste. The simplicity and computational efficiency of bilinear interpolation facilitates fast iterations in the design process, ensuring compatibility and continuity at region boundaries, thereby preventing stress concentrations and potential failure points. By enabling smooth transitions and precise fiber orientation, bilinear interpolation helps create advanced composite structures with superior mechanical properties, improved load distribution, and enhanced durability. To support these claims, relevant studies have demonstrated the effectiveness of interpolation-based formulations for modeling CFPs [28,29], and have highlighted the advantages of smoothly varying fiber orientation schemes over piecewise-constant or discrete approaches in terms of structural performance and manufacturability [30].

In the context of modeling CFPs in composite structures using a bilinear distribution, the angle at any point within a quadrilateral area can be interpolated based on the angles at the four corners of the area. To divide the spanwise panel into multiple design regions and write the equations for these regions while considering compatibility at the boundaries, we need to define the boundaries of the regions, ensure the angles at these boundaries are continuous for compatibility, and modify the bilinear interpolation equations for each region accordingly.

For a composite rectangular panel divided into n design regions, the fiber angle in each region is calculated using bilinear interpolation based on the fiber angles at the four corners of the region. Let the i-th region be defined by the following boundaries and corner fiber angles:

x_1^i, x_2^i : x-coordinates of the left and right boundaries,

y_1^i, y_2^i : y-coordinates of the bottom and top boundaries,

$T_1^i, T_2^i, T_3^i, T_4^i$: fiber angles at the bottom-left, top-left, top-right, and bottom-right corners, respectively.

Given that the span L is on the horizontal axis and the width b is on the vertical axis, the general bilinear interpolation formula for a quadrilateral region defined by points $(x_1^i, y_1^i), (x_2^i, y_1^i), (x_1^i, y_2^i), (x_2^i, y_2^i)$ with angles $T_1^i, T_2^i, T_3^i, T_4^i$, for each region can be expressed as follows:

$$\theta_i(x,y) = T_1^i(1-\mathrm{X}^i)(1-\Upsilon^i) + T_4^i\mathrm{X}^i(1-\Upsilon^i) + T_2^i(1-\mathrm{X}^i)\Upsilon^i + T_3^i\mathrm{X}^i\Upsilon^i$$

where,

$$\mathrm{X} = \frac{x - x_1^i}{x_2^i - x_1^i}, \qquad \Upsilon = \frac{y - y_1^i}{y_2^i - y_1^i} \tag{1}$$

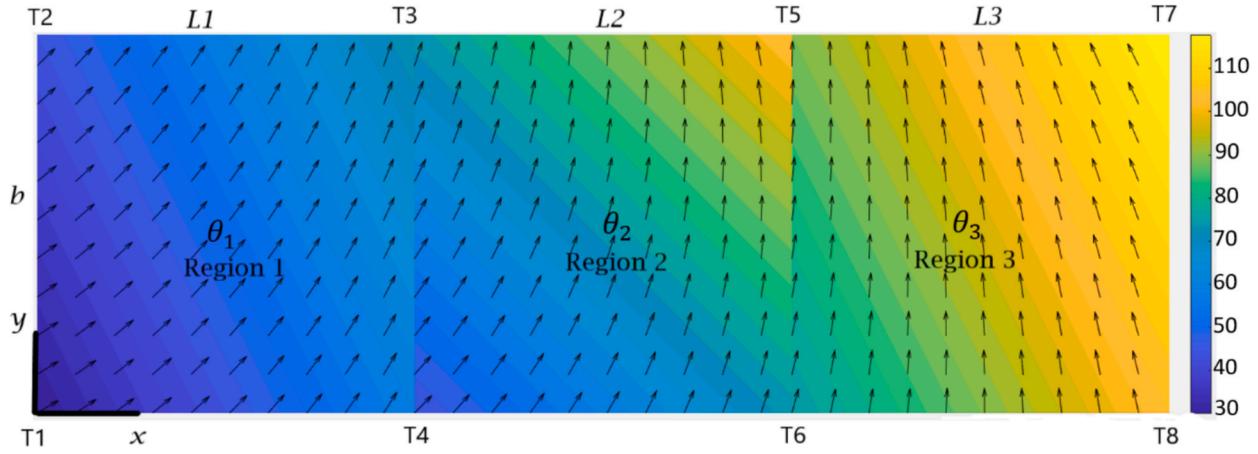

Fig. 1. Fiber orientation field across three design regions using bilinear interpolation. Colors indicate local fiber angles, and black arrows show fiber directions based on corner values T1–T8.

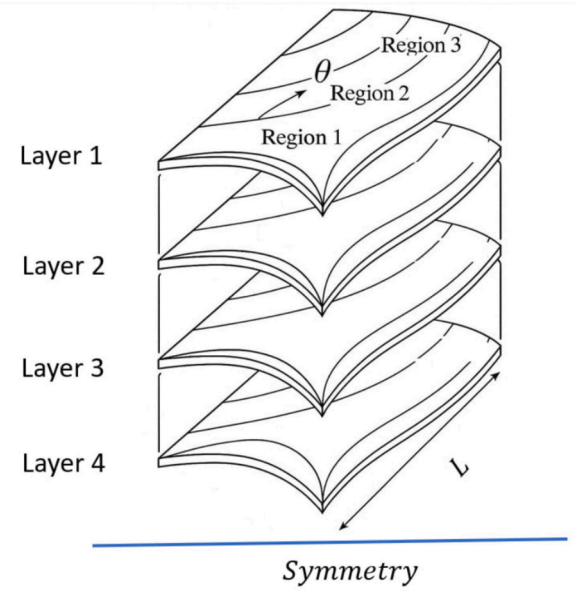

Fig. 2. Schematic representation of the eight-layered symmetric cylindrical composite panel. The figure illustrates the curvilinear fiber paths (θ) distributed across three distinct spanwise design regions (Region 1, Region 2, Region 3) within each layer.

The specific formulas for three regions panel, along with the total span L, width b, and the region span lengths, L_1, L_2 and L_3, are defined as follows for bilinear interpolation in each region:

Region 1:$0 \leqslant x \leqslant L_1$

For region 1, the corners are $(0,0),(L_1,0),(0,b),(L_1,b)$:

$$\theta_1(x,y) = T_1\left(1-\frac{x}{L_1}\right)\left(1-\frac{y}{b}\right) + T_4\frac{x}{L_1}\left(1-\frac{y}{b}\right) + T_2\left(1-\frac{x}{L_1}\right)\frac{y}{b} + T_3\frac{x}{L_1}\frac{y}{b} \tag{2}$$

Region 2:$L_1 \leqslant x \leqslant L_1 + L_2$

For region 2, the corners are $(L_1,0),(L_1+L_2,0),(L_1,b),(L_1+L_2,b)$:

$$\theta_2(x,y) = T_4\left(1-\frac{x-L_1}{L_2}\right)\left(1-\frac{y}{b}\right) + T_6\frac{x-L_1}{L_2}\left(1-\frac{y}{b}\right) + T_3\left(1-\frac{x-L_1}{L_2}\right)\frac{y}{b} + T_5\frac{x-L_1}{L_2}\frac{y}{b} \tag{3}$$

Region 3:$L_1 + L_2 \leqslant x \leqslant L$

For region 3, the corners are $(L_1+L_2,0),(L,0),(L_1+L_2,b),(L,b)$:

$$\theta_3(x,y) = T_6\left(1-\frac{x-L_1-L_2}{L_3}\right)\left(1-\frac{y}{b}\right) + T_8\frac{x-L_1-L_2}{L_3}\left(1-\frac{y}{b}\right) + T_5\left(1-\frac{x-L_1-L_2}{L_3}\right)\frac{y}{b} + T_7\frac{x-L_1-L_2}{L_3}\frac{y}{b} \tag{4}$$

Fig. 1 serves as a three regions example demonstrating the application of the presented bilinear interpolation formulation for modeling CFPs in composite laminates. The color bar on the right side of the figure represents the local fiber orientation angles (in degrees) across the composite panel surface. These angles are computed using bilinear interpolation based on the corner values T1 to T8, and are distributed over three design regions (Region 1, Region 2, and Region 3). The overlaid black arrows indicate the corresponding fiber directions at each point, visually reinforcing the smooth variation of fiber orientation throughout the panel. This legend provides a clear interpretation of how the interpolated angle field governs the curvilinear fiber layout in each region.

The panel is divided into three distinct regions along the spanwise direction to showcase how fiber orientations can be smoothly transitioned across different sections. Each region's fiber angles are interpolated from the angles specified at the corners, ensuring compatibility and continuity at the boundaries, as illustrated by the smooth gradient of arrow directions. The displayed equations indicate the bilinear interpolation formula used in each region, emphasizing the flexibility and precision of this method in defining fiber paths. This example is particularly relevant for applications using AFP techniques, where such precise control over fiber orientation is crucial for optimizing the structural integrity, mechanical performance, and manufacturing efficiency of composite materials.

The objective of the optimization strategy is to maximize the FNF of the eight-layer symmetric composite cylindrical panel illustrated in Fig. 2. In this study, the FNF refers specifically to the first vibrational mode of the composite panel, which is a critical performance metric in aerospace structures [31–33]. Maximizing the FNF helps avoid resonance with operational excitations such as unsteady aerodynamic loads, thereby enhancing dynamic stability, structural safety, and vibration resistance. The first mode often dominates the response of thin-walled components like fuselage and wing panels, making it an effective target for improving stiffness-to-mass efficiency. Additionally, higher FNFs support compliance with aerospace certification standards that require minimum frequency thresholds to prevent coupling with control system dynamics [34].

This goal may be achieved by optimizing the fiber path/orientation within each layer. In the present study, an eight layered symmetric cylindrical panel is assumed with the following stacking sequence.

$$\begin{aligned}
&\left[\Theta^1/\Theta^2/\Theta^3/\Theta^4\right]_{sym}\\
&\Theta^1 \sim \theta_1^1 \to \langle T_1^1, T_2^1, T_3^1, T_4^1\rangle, \theta_2^1 \to \langle T_3^1, T_4^1, T_5^1, T_6^1\rangle, \theta_3^1 \to \langle T_5^1, T_6^1, T_7^1, T_8^1\rangle\\
&\Theta^2 \sim \theta_1^2 \to \langle T_1^2, T_2^2, T_3^2, T_4^2\rangle, \theta_2^2 \to \langle T_3^2, T_4^2, T_5^2, T_6^2\rangle, \theta_3^2 \to \langle T_5^2, T_6^2, T_7^2, T_8^2\rangle\\
&\Theta^3 \sim \theta_1^3 \to \langle T_1^3, T_2^3, T_3^3, T_4^3\rangle, \theta_2^3 \to \langle T_3^3, T_4^3, T_5^3, T_6^3\rangle, \theta_3^3 \to \langle T_5^3, T_6^3, T_7^3, T_8^3\rangle\\
&\Theta^4 \sim \theta_1^4 \to \langle T_1^4, T_2^4, T_3^4, T_4^4\rangle, \theta_2^4 \to \langle T_3^4, T_4^4, T_5^4, T_6^4\rangle, \theta_3^4 \to \langle T_5^4, T_6^4, T_7^4, T_8^4\rangle
\end{aligned} \tag{5}$$

2.1.1. Maximum allowable curvature (MAC)

The Maximum Allowable Curvature (MAC) is a critical constraint in the design optimization of CFP, particularly in composite panel structures manufactured via AFP. MAC directly affects the manufacturability, structural integrity, and performance of the final component. Excessive curvature can exceed the material's bending capacity, leading to fiber wrinkling, misalignment, or breakage during the placement process, which in turn degrades mechanical properties and compromises load-carrying capacity [35,36]. Since AFP is constrained by factors such as tow stiffness and machine head geometry, maintaining fiber curvature within allowable limits ensures that the designed fiber paths are not only structurally efficient but also feasible and cost-effective to produce. Incorporating MAC as an optimization constraint minimizes the risk of manufacturing defects, reduces production rework, and improves the long-term reliability of variable stiffness laminates. Recent studies have emphasized the significance of MAC in ensuring practical and robust CFP designs [37,38]. By incorporating the MAC as a constraint in the optimization, designers can achieve a balance between structural efficiency, manufacturability, and cost-effectiveness, thereby minimizing production risks and ensuring long-term reliability of the composite component. Equations (6) and (7) give the MAC (K_{max}) in Cartesian coordinates while the bilinear interpolation is used to design the CFP. The curvature $K(x,y)$ at a point is defined as:

$$K(x,y) = \sqrt{\left(\frac{\partial\theta}{\partial x}\right)^2 + \left(\frac{\partial\theta}{\partial y}\right)^2} \tag{6}$$

While, substituting the gradients gives the MAC $K_{max} = \max(K(x,y))$.

$$K(x,y) = \sqrt{\left[\frac{1}{x_2-x_1}\left((T_4-T_1)\frac{y_2-y}{y_2-y_1} + (T_3-T_2)\frac{y-y_1}{y_2-y_1}\right)\right]^2 + \left[\frac{1}{y_2-y_1}\left((T_2-T_1)\frac{x_2-x}{x_2-x_1} + (T_3-T_4)\frac{x-x_1}{x_2-x_1}\right)\right]} \tag{7}$$

2.1.2. Optimization study

This section introduces the Multi-Region Optimization (MRO) problem, including its objective, design variables, and constraints.

Table 1
Optimization problem.

Objective: Maximizing the FNF	
Variables: Length of regions, $0 < L_i < L, i = 1,2,3$	
Fiber angle in bilinear interpolation, $0^\circ \leq T_k \leq 180^\circ, k = 1, \cdots, 8$	
Constraints: Maximum allowable curvature, $K_{\max} < 3.2$	

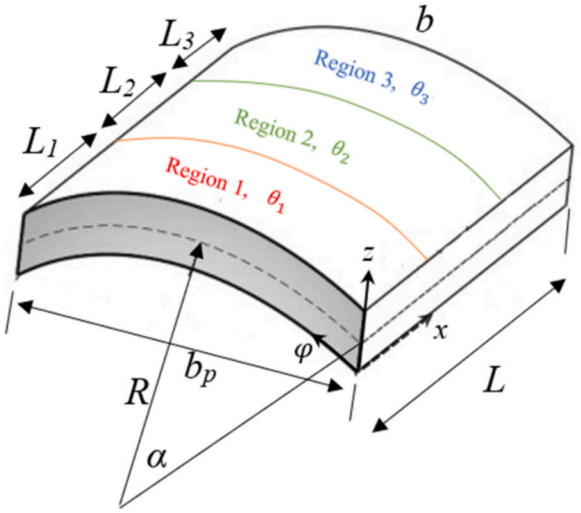

Fig. 3. Geometry of the cylindrical composite panel, showing the curvilinear fiber path design over three sub-regions defined along the spanwise direction. Each region is governed by a distinct fiber orientation function θ_i, where i= 1,2,3, allowing spatially varying fiber paths. Key geometric parameters include total span b, panel length L, panel radius R, arc angle α, projected base length bp, and regional spans L_1,L_2,L_3.

The cost function for the optimization algorithm is defined as the FNF, with the objective of maximizing its value. The design variables consist of the eight fiber angles determined by bilinear interpolation for three regions across the four composite layers, resulting in a total of 24 variables. Additionally, three variables are derived from the lengths of each region in each layer. These variables can be continuously adjusted within specific predefined intervals. Considering the symmetry of the composite layups, the optimization process specifically targets the fiber angles of the first four layers.

In summary, the optimization problem is characterized by its objective function, constraints, and variable intervals, as detailed in Table 1.

where, K_{max}, the MAC, depends on the feed rate of the tow-placement machines. The curvature limit of $K_{max} = 3.2\ \text{m}^{-1}$ used in the GA-based optimization was selected based on practical manufacturing constraints associated with AFP [13,39–41]. This value corresponds to a minimum curvature radius of approximately 312.5 mm, aligning with industry-reported limits (typically 2.5–5.0 m^{-1}) depending on tow width and material type [36]. It offers a balanced trade-off between manufacturability and design flexibility, ensuring the optimized fiber paths are both feasible for production and structurally effective.

In this study, optimal lamination angles are determined using a GA. The GA begins with a randomly generated population of individuals in a generation and evolves toward a solution by assessing fitness, selecting multiple individuals from the current population, and modifying them to create a new population. The algorithm terminates when a satisfactory fitness level is reached for the population, with the fittest chromosome designated as the optimal solution.

2.2. Governing equation of motion

The governing equations of motion for the presented panel structure were derived and analyzed in the authors' previous work [4]. Detailed formulations, including the governing equations, geometric mapping, and the application of the GDQ method, are available in Refs [4,42].

Moderately thick panels are represented schematically in Fig. 3 with three distinct design regions, where they feature an orthogonal fixed curvilinear coordinate system (x,φ,z) at the panel's corner. This system is defined by parameters; width length b, panel span L, radius of curvature R, and thickness h.

The displacement field (u,v,w) at any arbitrary point on the panel's mid-surface, with respect to position coordinates (x, φ, z) and time t, can be expressed as follows:

$$\begin{aligned} u(x,y,z,t) &= u_0(x,y,t) + z\phi_x(x,y,t) \\ v(x,y,z,t) &= v_0(x,y,t) + z\phi_\varphi(x,y,t) \\ w(x,y,z,t) &= w_0(x,y,t) \end{aligned} \tag{8}$$

Here, the symbols u_0, v_0 and w_0 denote mid-plane deformations in the x, φ and z directions, while ϕ_x and ϕ_φ represent rotations of the surface normal about the φ and x axes, respectively. Now, let's consider the fully nonlinear Green strain–displacement relations for an elastic cylindrical panel including normal and shear strains are as follows,

$$\begin{aligned} \varepsilon_{xx} &= \frac{\partial u_0}{\partial x} + \frac{1}{2}\left(\left(\frac{\partial u_0}{\partial x}\right)^2 + \left(\frac{\partial v_0}{\partial x}\right)^2 + \left(\frac{\partial w_0}{\partial x}\right)^2\right) + z\frac{\partial \phi_x}{\partial x} + \frac{z^2}{2}\frac{\partial^2 \phi_x}{\partial x^2} \\ \varepsilon_{\varphi\varphi} &= \frac{\partial v_0}{\partial \varphi} + \frac{w_0}{R} + \frac{1}{2}\left(\left(\frac{\partial u_0}{\partial \varphi}\right)^2 + \left(\frac{\partial v_0}{\partial \varphi}\right)^2 + \left(\frac{\partial w_0}{\partial \varphi}\right)^2\right) + z\left(\frac{\partial \phi_\varphi}{\partial \varphi} + \frac{\phi_\varphi}{R}\right) + \\ &\quad \frac{z^2}{2}\left(\frac{\partial^2 \phi_\varphi}{\partial \varphi^2} + \frac{\partial \phi_\varphi}{R\partial \varphi}\right) \\ \gamma_{x\varphi} &= \frac{1}{2}\left(\frac{\partial u_0}{\partial \varphi} + \frac{\partial v_0}{\partial x}\right) + \frac{1}{2}\left[\frac{\partial u_0}{\partial x}\frac{\partial u_0}{\partial \varphi} + \frac{\partial v_0}{\partial x}\frac{\partial v_0}{\partial \varphi} + \frac{\partial w_0}{\partial x}\frac{\partial w_0}{\partial \varphi}\right] + z\left(\frac{\partial \phi_x}{\partial \varphi} + \frac{\partial \phi_\varphi}{\partial x}\right) + \\ &\quad \frac{z^2}{2}\left(\frac{\partial^2 \phi_x}{\partial \varphi^2} + \frac{\partial^2 \phi_\varphi}{\partial x^2}\right) \\ \gamma_{xz} &= \frac{\partial w_0}{\partial x} - \phi_x + \frac{1}{2}\left[\frac{\partial u_0}{\partial x}\frac{\partial w_0}{\partial x} + \frac{\partial v_0}{\partial x}\frac{\partial w_0}{\partial x}\right] + z\frac{\partial \phi_x}{\partial x} + \frac{z^2}{2}\frac{\partial^2 \phi_x}{\partial x^2} \\ \gamma_{x\varphi} &= \frac{\partial w_0}{\partial \varphi} - \phi_\varphi + \frac{1}{2}\left[\frac{\partial u_0}{\partial \varphi}\frac{\partial w_0}{\partial \varphi} + \frac{\partial v_0}{\partial \varphi}\frac{\partial w_0}{\partial \varphi}\right] + z\left(\frac{\partial \phi_\varphi}{\partial \varphi} + \frac{\phi_\varphi}{R}\right) + \frac{z^2}{2}\left(\frac{\partial^2 \phi_\varphi}{\partial \varphi^2} + \frac{\partial \phi_\varphi}{R\partial \varphi}\right) \end{aligned} \tag{9}$$

The governing equations of motion for the cylindrical panel are obtained by constructing the structure's Hamiltonian as follows,

$$\int_{t_1}^{t_2} \delta(T - U + W_{ext})\,\mathrm{d}t = 0 \tag{10}$$

The kinetic and potential energies of the panel are denoted as T and U, and non-conservative external forces in this study are disregarded. The panel's kinetic energy is defined as:

$$T = \int_V \frac{1}{2}\rho(\dot{u}_x^2 + \dot{u}_\varphi^2 + \dot{u}_z^2) R\mathrm{d}z\mathrm{d}x\mathrm{d}\varphi \tag{11}$$

The over dot symbol signifies differentiation with respect to the temporal coordinate, and the mass density of the layer is denoted by ρ. When the displacement field from Eq. (8) is inserted into the kinetic energy expression given in Eq. (11) and some manipulations are performed, the following variational representation of the kinetic energy is obtained.

$$\delta T = \int_0^L \int_0^b \left[\begin{array}{c} I_0(\ddot{u}_0\delta u_0 + \ddot{v}_0\delta v_0 + \ddot{w}_0\delta w_0) \\ +I_1(\ddot{\phi}_x\delta u_0 + \ddot{\phi}_\varphi\delta v_0 + \ddot{u}_0\delta\phi_x + \ddot{v}_0\delta\phi_\varphi) + I_2(\ddot{\phi}_x\delta\phi_x + \ddot{\phi}_\varphi\delta\phi_\varphi) \end{array}\right] R\mathrm{d}x\mathrm{d}\varphi, \tag{12}$$

The mass moments of inertia are denoted as $I_j; j = 0, 1, 2$ and are defined in Ref [4].

The next relation needed for the construction of the system's Hamiltonian is the expression for elastic strain potential energy. The expression for total potential energy is defined as follows:

$$U = \int_V \frac{1}{2}(\sigma_{xx}\varepsilon_{xx} + \sigma_{\varphi\varphi}\varepsilon_{\varphi\varphi} + 2\sigma_{x\varphi}\varepsilon_{x\varphi} + 2\sigma_{xz}\varepsilon_{xz} + 2\sigma_{\varphi z}\varepsilon_{\varphi z})\, R\mathrm{d}z\mathrm{d}x\mathrm{d}\varphi \tag{13}$$

After some manipulation and substituting the partial expressions for kinematic and potential energy into Hamilton's principle, we derive the following explicit integral expression for the governing equation of motion for the cylindrical panel geometry,

$$\int_0^L \int_0^b \left[\begin{array}{c} (I_0\ddot{u}_0 + I_1\ddot{\phi}_x)\delta u_0 + \mu_1\delta u_{0,x} + \mu_2\delta u_{0,\varphi} + (\mu_3 + I_1\ddot{\phi}_\varphi + I_0\ddot{v}_0)\delta v_0 \\ +\mu_4\delta v_{0,x} + \mu_5\delta v_{0,\varphi} + (\mu_6 + I_0\ddot{w}_0)\delta w_0 + \mu_7\delta w_{0,x} + \mu_8\delta w_{0,\varphi} \\ +(\mu_9 + I_1\ddot{u}_0 + I_2\ddot{\phi}_x)\delta\phi_x + \mu_{10}\delta\phi_{x,x} + \mu_{11}\delta\phi_{x,\varphi} \\ +(\mu_{12} + I_2\ddot{\phi}_\varphi + I_1\ddot{v}_0)\delta\phi_\varphi + \mu_{13}\delta\phi_{\varphi,x} + \mu_{14}\delta\phi_{\varphi,\varphi} \end{array}\right] R\mathrm{d}x\mathrm{d}\varphi = 0 \tag{14}$$

where $\mu_i; i = 1, 2, \ldots, 14$ are defined in Ref [4].

A geometric mapping, inspired by Kurtaran [36], is employed to streamline numerical integrations. Through this mapping, the curvilinear coordinate system is transformed into a bi-unit square domain. Detailed discussions on the mapping relations and

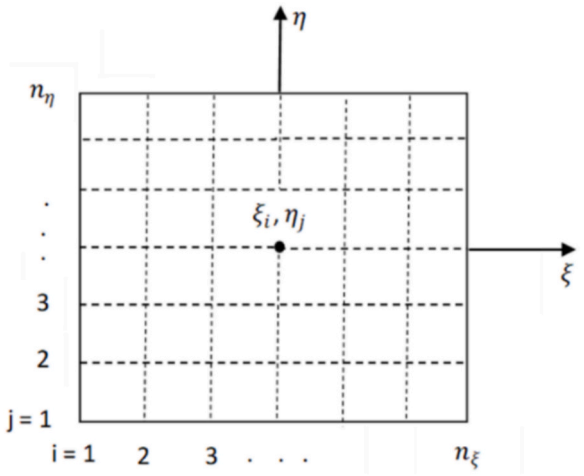

Fig. 4. Schematic of the grid point distribution used in the numerical implementation of the GDQ method, shown in the local coordinate system (ξ,η).

sequences can be found in the work by Kurtaran [36].

2.3. Solution methodology and GDQ method

The solution method comprises the discretization of the curvilinear domain using the Gauss-Lobatto grid point distribution, enabling the application of the GDQ method to compute partial derivatives at grid points and evaluate the integrals in the governing equation of motion. To compute the derivatives of the field variables, an enhanced GDQ method is employed. Before applying the GDQ method, the laminated panel is discretized using grid points, where the field variables and their derivatives are computed. In accordance with the GDQ method, the *r*th-order derivative of a function $f(\xi)$ at n discrete grid points can be expressed as,

$$\left(\frac{\partial f^r(\xi)}{\partial \xi^r}\right)_{\xi_i} = \sum_{j=1}^{n} C_{ij}^{(r)} f_j \tag{15}$$

The discrete points within the computational domain are denoted by ξ_i, and the weighting coefficients and function values at these points are represented by $C_{ij}(r)$ *and* f_j, respectively. An explicit formula for the weighting coefficients, based on the Lagrange polynomial for the first-order derivative ($r = 1$), is given as follows,

$$C_{ij}^{(1)} = \frac{\Phi(\xi_i)}{(\xi_i - \xi_j)\Phi(\xi_j)} \; (i \neq j) \; where, \Phi(\xi_i) = \prod_{j=1}^{n} (\xi_i - \xi_j) \quad (i \neq j) \tag{16}$$

For higher-order derivative weighing coefficient matrix components, the GDQ method introduces the following recursive relations:

$$C_{ij}^{(r)} = r\left[C_{ii}^{(r-1)} C_{ij}^{(1)} - \frac{C_{ij}^{(r-1)}}{\xi_i - \xi_j}\right] (i \neq j) \; and, \; C_{ii}^{(r)} = -\sum_{\substack{j=1 \\ i \neq j}}^{n} C_{ij}^{(r)} \tag{17}$$

As illustrated in Fig. 4, the partial derivatives at a point (ξ_i, η_j) can be defined as follows, with the grid numbers in the n_ξ and n_η directions being denoted as the ξ and η respectively.

$$\begin{aligned} &\left(\frac{\partial f^r(\xi,\eta)}{\partial \xi^r}\right)_{\xi_i,\eta_j} = \sum_{k=1}^{n_\xi} C_{kj}^{(r)} f_{kj}, \qquad \left(\frac{\partial f^s(\xi,\eta)}{\partial \eta^s}\right)_{\xi_i,\eta_j} = \sum_{m=1}^{n_\eta} C_{im}^{(s)} f_{im} \\ &\left(\frac{\partial f^{(r+s)}(\xi,\eta)}{\partial \xi^r \partial \eta^s}\right)_{\xi_i,y_j} = \frac{\partial^r}{\partial \xi^r}\left(\frac{\partial^s f}{\partial \eta^s}\right) = \sum_{k=1}^{n_\xi} \sum_{m=1}^{n_\eta} C_{kj}^{(r)} C_{im}^{(s)} f_{km} \end{aligned} \tag{18}$$

Please note that the variables r and s represent the derivative orders concerning the variables ξ and η, respectively.

One essential point to note is that when calculating the partial derivatives of a general function f with respect to the variables x, φ, the GDQ method is applied at grid points in the following manner:

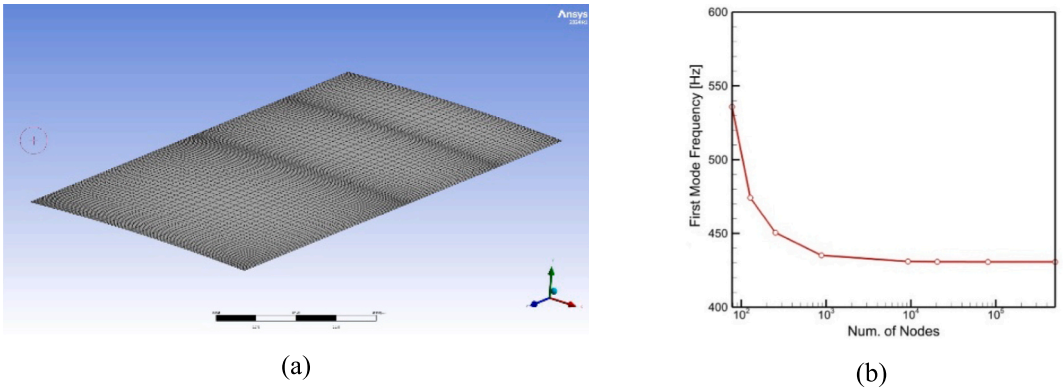

Fig. 5. a) ansys mesh configuration and b) convergence study for the cylindrical panel under case study boundary conditions (CCCC), with $R = 5$, and $L/b = 2$.

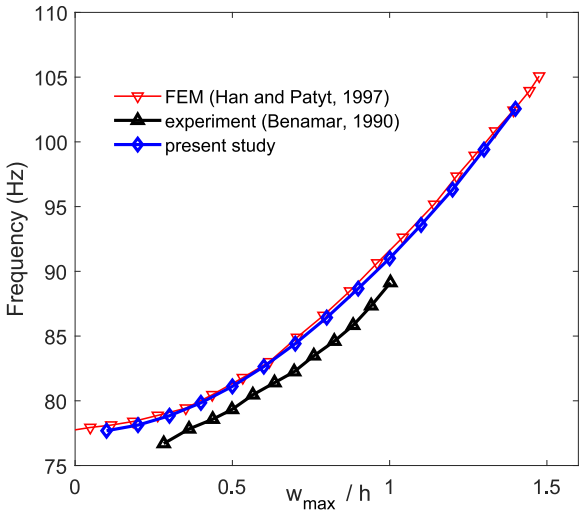

Fig. 6. Comparison of the geometrically nonlinear fundamental resonant frequencies as a function of the normalized maximum transverse displacement.

Table 2
Geometric and material properties of the composite cylindrical panel.

$L(m)$	$b(m)$	R	$h(m)$	E_1 (Gpa)	E_2 (Gpa)	G_{12} (Gpa)	G_{13} (Gpa)	G_{23} (Gpa)	υ_{12}	ρ (kg/m^3)
1	0.5,1	5,10	$L/100$	*173*	7.2	3.76	*3.76*	3.76	0.29	1540

$$\left(\frac{\partial f}{\partial x}\right)_{ij} = \frac{1}{J_{ij}}\left[\left(\frac{\partial \varphi}{\partial \eta}\right)_{ij}\sum_{k=1}^{n_\xi} C_{kj}^{(1)} f_{kj} - \left(\frac{\partial \varphi}{\partial \xi}\right)_{ij}\sum_{m=1}^{n_\eta} C_{im}^{(1)} f_{im}\right]$$
$$\left(\frac{\partial f}{\partial \varphi}\right)_{ij} = \frac{1}{J_{ij}}\left[\left(\frac{\partial x}{\partial \xi}\right)_{ij}\sum_{m=1}^{n_\eta} C_{im}^{(1)} f_{im} - \left(\frac{\partial x}{\partial \eta}\right)_{ij}\sum_{k=1}^{n_\xi} C_{kj}^{(1)} f_{kj}\right] \tag{19}$$

where J_{ij} is the Jacobian of the transformation given in Ref [36].

2.4. Nonlinear eigenvalue analysis

The governing equation from Eq. (14) is solved using the GDQ method to determine the structural matrices and associated FNAF. The nonlinear system of equations is established in the following form,

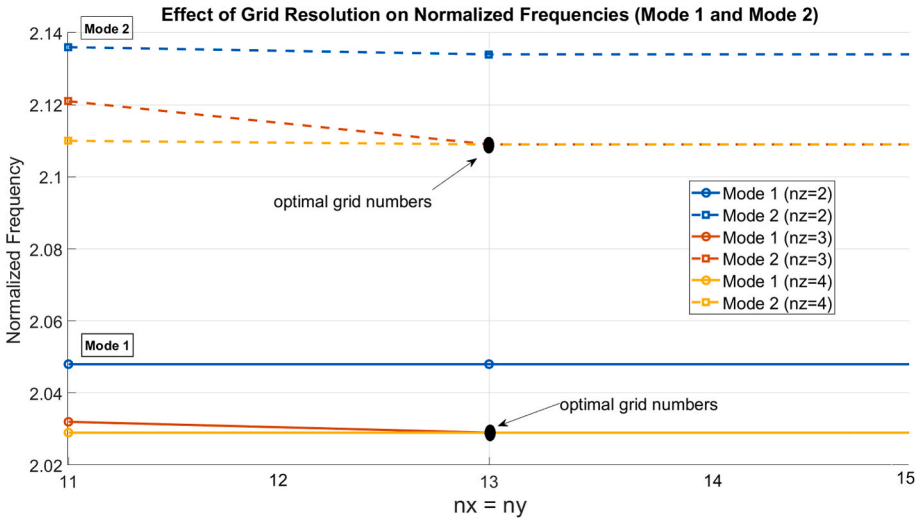

Fig. 7. GDQ grid convergence study showing the variation of normalized frequencies for Mode 1 and Mode 2 with respect to in-plane discretization ($n_x = n_y$) and thickness layers (n_z).

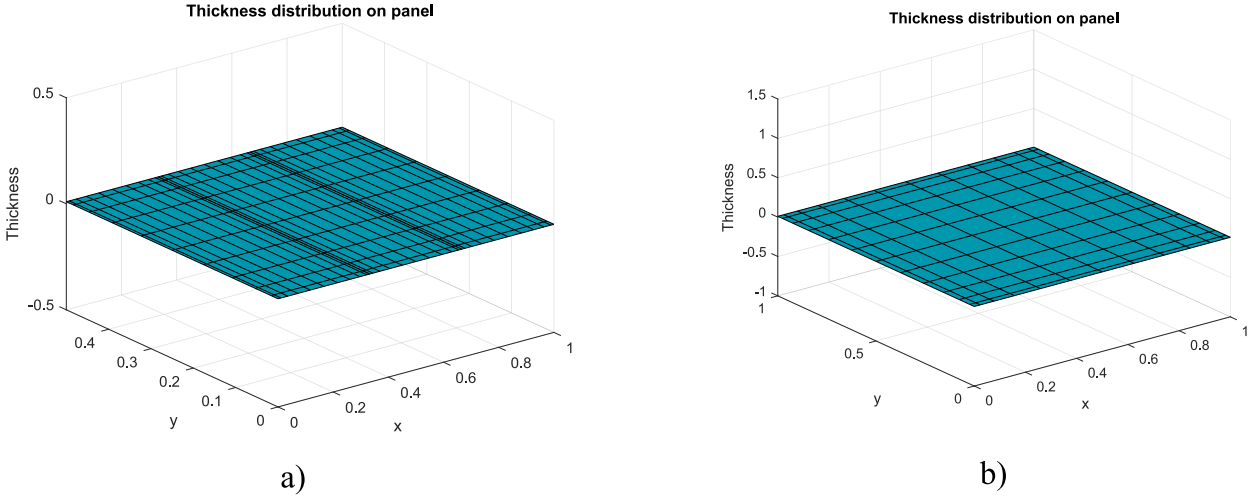

Fig. 8. Grid point distribution over the panel's surface for (a) Multi-Region CFP (M−CFP) and (b) Single-Region CFP (S-CFP).

$$\mathbf{M}\ddot{\boldsymbol{u}} + \left[\mathbf{K}_{\mathrm{L}} + \mathbf{K}_{NL}^{1}(\boldsymbol{u}) + \mathbf{K}_{NL}^{2}(\boldsymbol{u}^{2})\right]\boldsymbol{u} = \mathbf{0} \tag{20}$$

where, the linear and nonlinear stiffness matrices are represented as $\mathbf{K}_{\mathrm{L}}$, $\mathbf{K}_{NL}^{1}(\boldsymbol{u})$ and $\mathbf{K}_{NL}^{2}(\boldsymbol{u}^{2})$. An imposed harmonic vibration response is assumed to take the following form,

$$\boldsymbol{u} = \bar{\boldsymbol{u}}\sin(\omega \mathrm{t}) \tag{21}$$

By inserting Eq. (21) into Eq. (20), the expanded representation of the governing equation is structured as,

$$-\omega^{2}\mathbf{M}\bar{\boldsymbol{u}}\sin(\omega \mathrm{t}) + \left[\mathbf{K}_{\mathrm{L}} + \mathbf{K}_{NL}^{1}(\bar{\boldsymbol{u}}\sin(\omega \mathrm{t})) + \mathbf{K}_{NL}^{2}\left(\bar{\boldsymbol{u}}^{2}\sin^{2}(\omega \mathrm{t})\right)\right]\bar{\boldsymbol{u}}\sin(\omega \mathrm{t}) = \mathbf{0} \tag{22}$$

Here, the nonlinear stiffness matrices $\mathbf{K}_{NL}^{1}(\boldsymbol{u})$ and $\mathbf{K}_{NL}^{2}(\boldsymbol{u}^{2})$ are dependent on time.

2.4.1. Simplification for residual definition

The left-hand side term in Eq. (22) is defined as Γ, leading to the expression:

$$\Gamma = -\omega^{2}\mathbf{M}\bar{\boldsymbol{u}}\sin(\omega \mathrm{t}) + \left[\mathbf{K}_{\mathrm{L}} + \mathbf{K}_{NL}^{1}(\bar{\boldsymbol{u}}\sin(\omega \mathrm{t})) + \mathbf{K}_{NL}^{2}\left(\bar{\boldsymbol{u}}^{2}\sin^{2}(\omega \mathrm{t})\right)\right]\bar{\boldsymbol{u}}\sin(\omega \mathrm{t}) \tag{23}$$

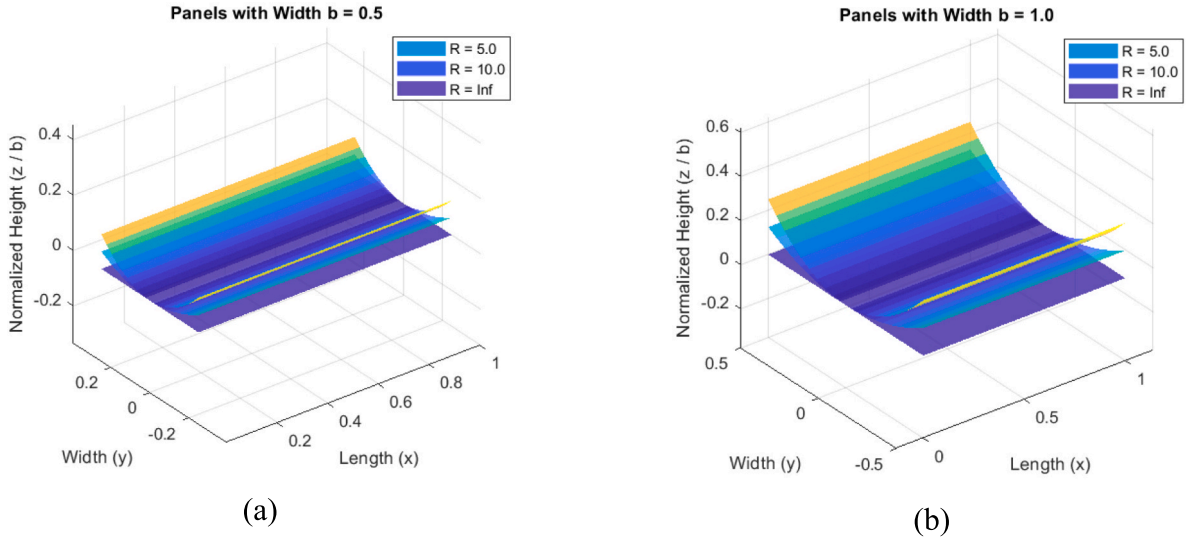

Fig. 9. Geometrical representation of the composite panel for different aspect ratios and radii of curvature. Subfigure (a) shows the panel with aspect ratio $L/b = 2$, and (b) shows $L/b = 1$, each plotted for three different radii: $R = 5$, $R = 10$, and $R=\infty$ (flat panel).

Table 3
Algorithm (GA) parameter settings for different search strategies in the optimization process, outlining key control variables.

Parameter	Global Search	Balanced Search	Local Search
Generations	100	50	50
Population Size	70	70	70
Mutation Rate (%)	5	5	5
Mutation Std. Dev	0.100 (fixed)	0.050 → 0.010	0.020 → 0.001
Crossover Method	Uniform / Sim. Binary (50 % each), 1-point, distribution index = 2.0		
Selection Method	Stochastic Selection with Linear Ranking		

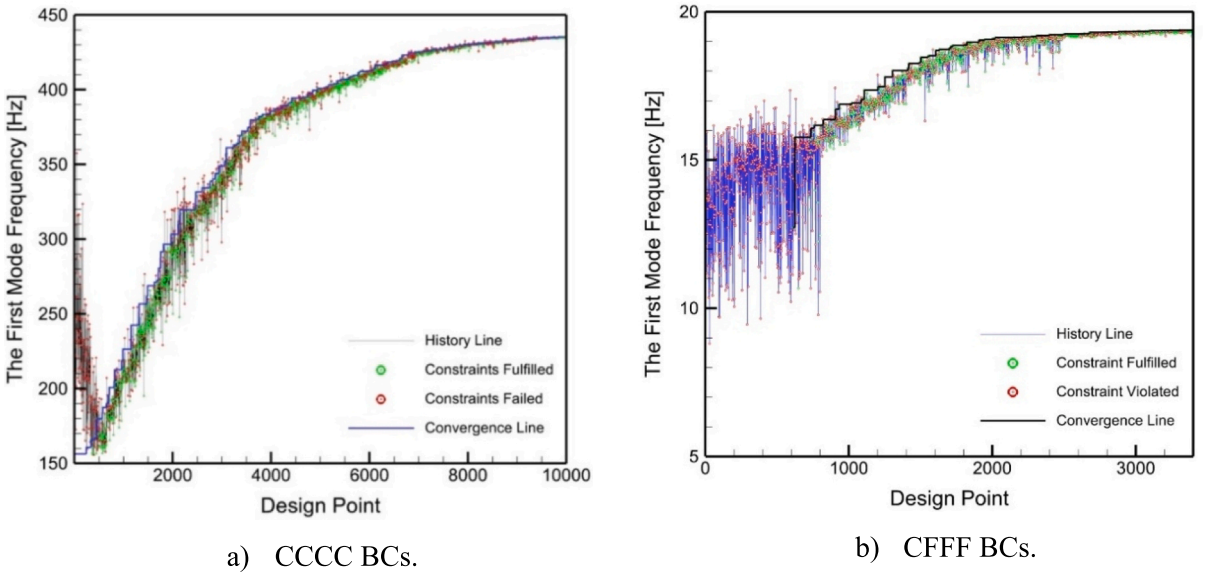

Fig. 10. GA optimizer convergence history showing the evolution of the first mode frequency [Hz] over 10,000 design evaluations. a) CCCC BCs. and b) CFFF BCs.

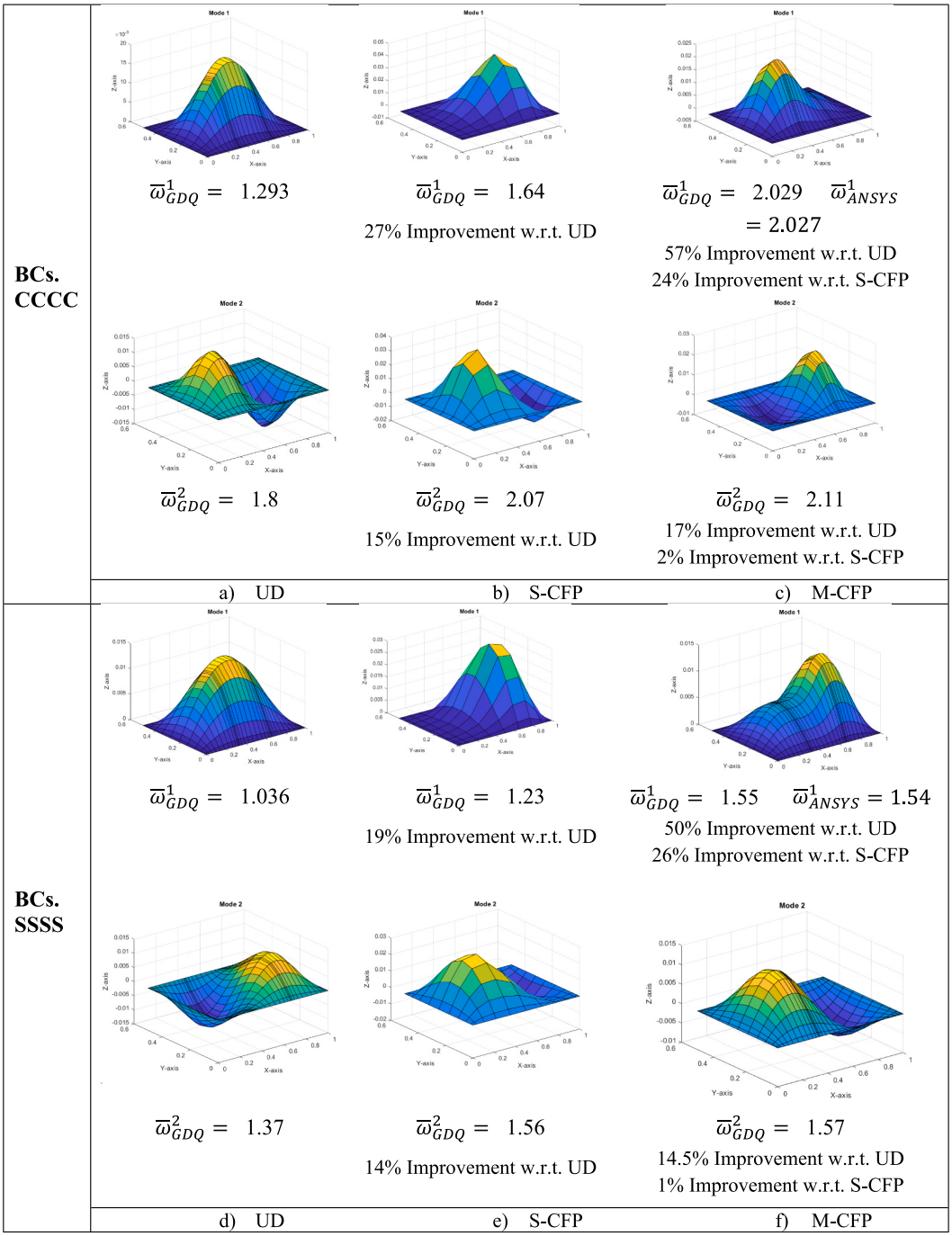

Fig. 11. Comparison of the fundamental natural frequency (FNF) and second mode shapes for panels with CCCC (a–c), SSSS (d–f), and CFFF (g–i) boundary conditions, using three configurations: unidirectional (UD), single-region curvilinear fiber path (S-CFP), and multi-region curvilinear fiber path (M−CFP). Results are shown for a cylindrical panel with $R = 5$ and $L/b = 2$, highlighting performance improvements of S-CFP and M−CFP over the conventional UD design.

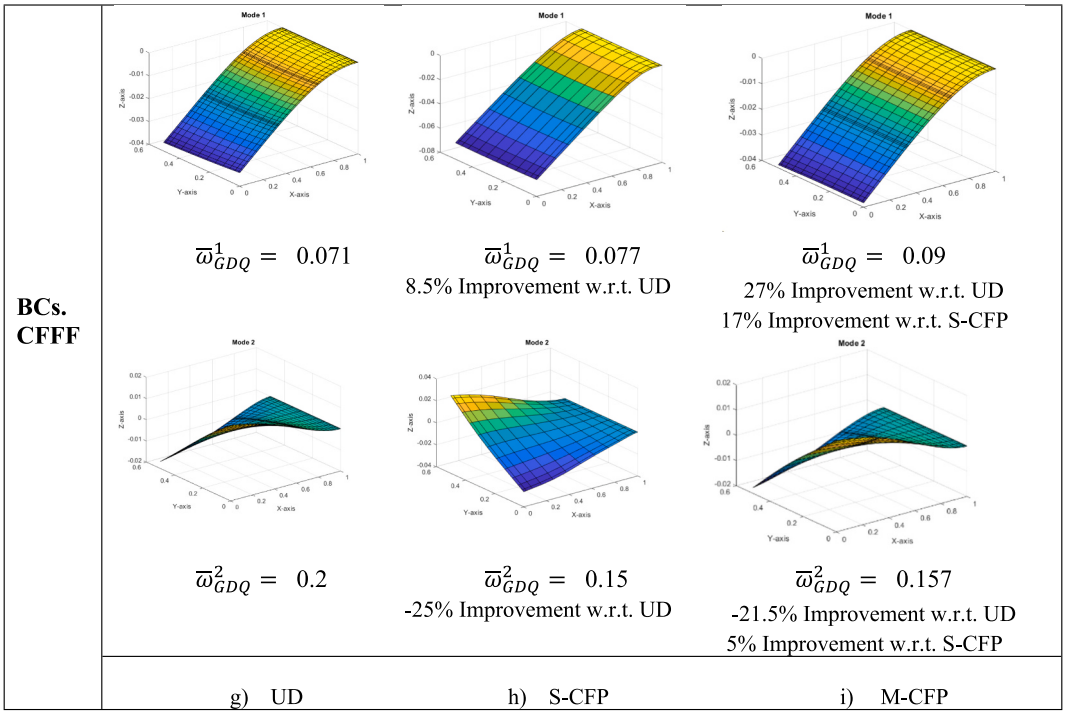

Fig. 11. (*continued*).

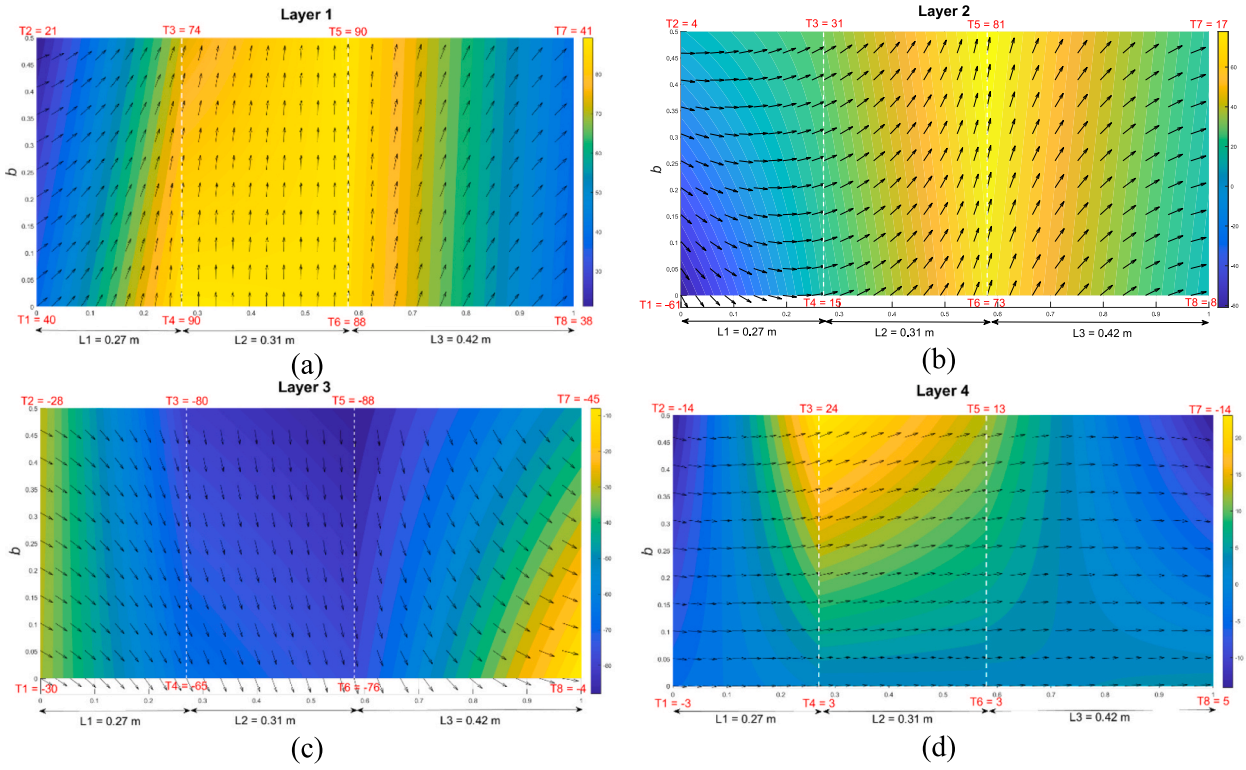

Fig. 12. Layer stacking sequences and designed fiber angles for the panel with CCCC BCs., $R = 5$, and $L/b = 2$. Subfigures (a–d) correspond to Layer 1 through Layer 4, respectively.

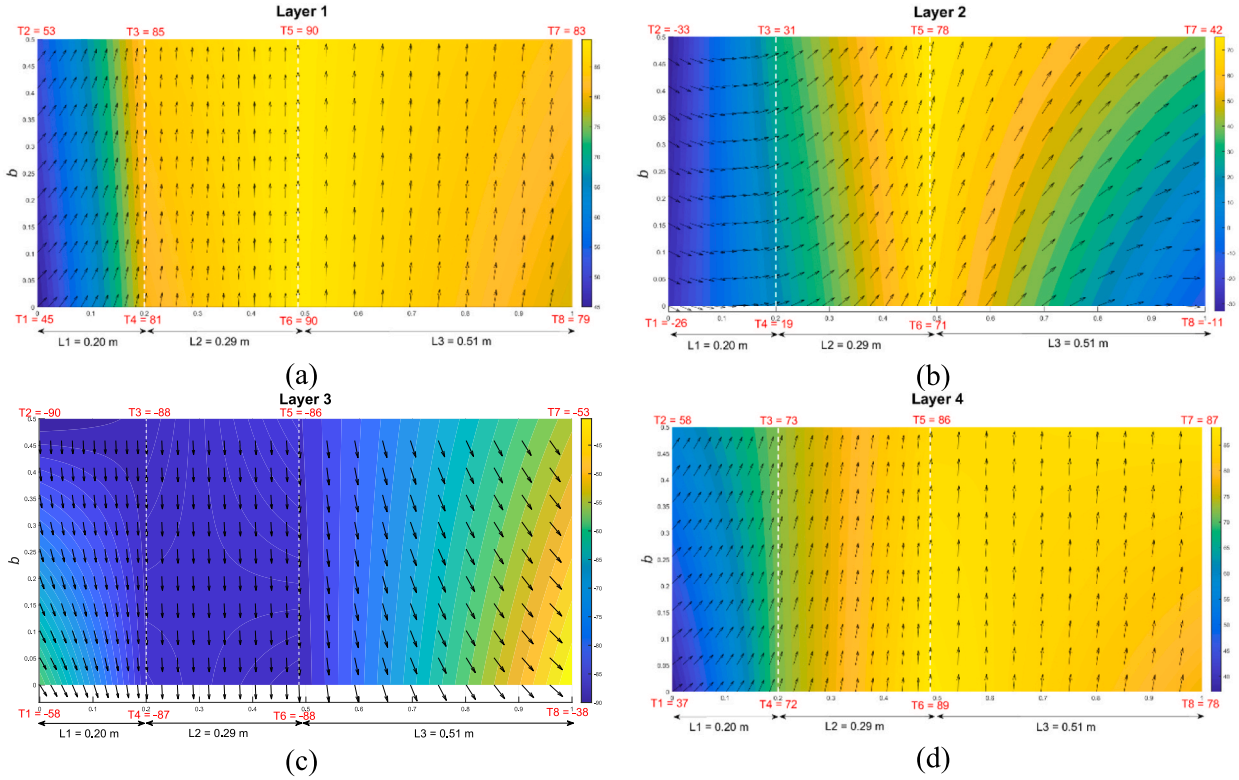

Fig. 13. Layer stacking sequences and designed fiber angles for the panel with SSSS BCs., $R = 5$, and $L/b = 2$. Subfigures (a–d) correspond to Layer 1 through Layer 4, respectively.

Integrating this term over one period of harmonic motion, and using the property,

$$\int_0^T \sin(\omega t)\mathrm{d}t = 0, T = \frac{2\pi}{\omega} \tag{24}$$

leads to the eigenvalue problem,

$$\left[-\omega^2\mathbf{M} + (\mathbf{K}_{\mathrm{L}} + \frac{8}{3\pi}\mathbf{K}_{NL}^1 + \frac{3}{4}\mathbf{K}_{NL}^2)\right]\bar{\boldsymbol{u}} = 0 \tag{25}$$

Solving Eq. (25) yields the nonlinear eigenfrequencies ω_{NL}, which are dependent on the amplitude $\bar{\mathbf{u}}$. Unlike linear eigenvalue problems, where a single eigenvalue is computed for each mode, the nonlinear eigenvalue problem results in multiple eigenvalues corresponding to different amplitudes $\bar{\mathbf{u}}$, reflecting the amplitude-dependent stiffness of the system. This formulation clarifies and verifies the original equations, ensuring both accuracy and clarity while accommodating nonlinear effects.

3. Result and discussion

3.1. Validation of the solution method

In this study, ANSYS ACP is utilized to validate composite panel geometrical linear model, the proposed solution theory and the application of the proposed CFP model. The process involves incorporating Python code within the ANSYS environment. This Python code is integrated into the solver, where it retrieves relevant values, calculates the fiber angle for each element, and subsequently employs these values as a spatial interpolation table within ANSYS ACP. This automated approach ensures accurate fiber angle distribution across the panel, enhancing the precision of the modeling and analysis process. Fig. 5 shows mesh configuration and convergence study for the cylindrical panel under case study boundary conditions (CCCC), with $R = 5$ and $L/b = 2$. The left image shows the finite element mesh used in ANSYS, while the right plot presents the variation of the first mode frequency with respect to the number of nodes, demonstrating convergence.

To validate the model accounting for geometric nonlinearity, Fig. 6 presents a comparison between the FANF obtained in this study and the results from Han and Petyt [42] as well as Benamar [43], focusing on an isotropic rectangular plate. The plate's dimensions measure $L = 0.486$ m, $b = 0.3229$ m, and $h = 1.2$ mm, and it possesses mechanical properties of $E = 210$ GPa and $\rho = 7800$ kg/m^3. The

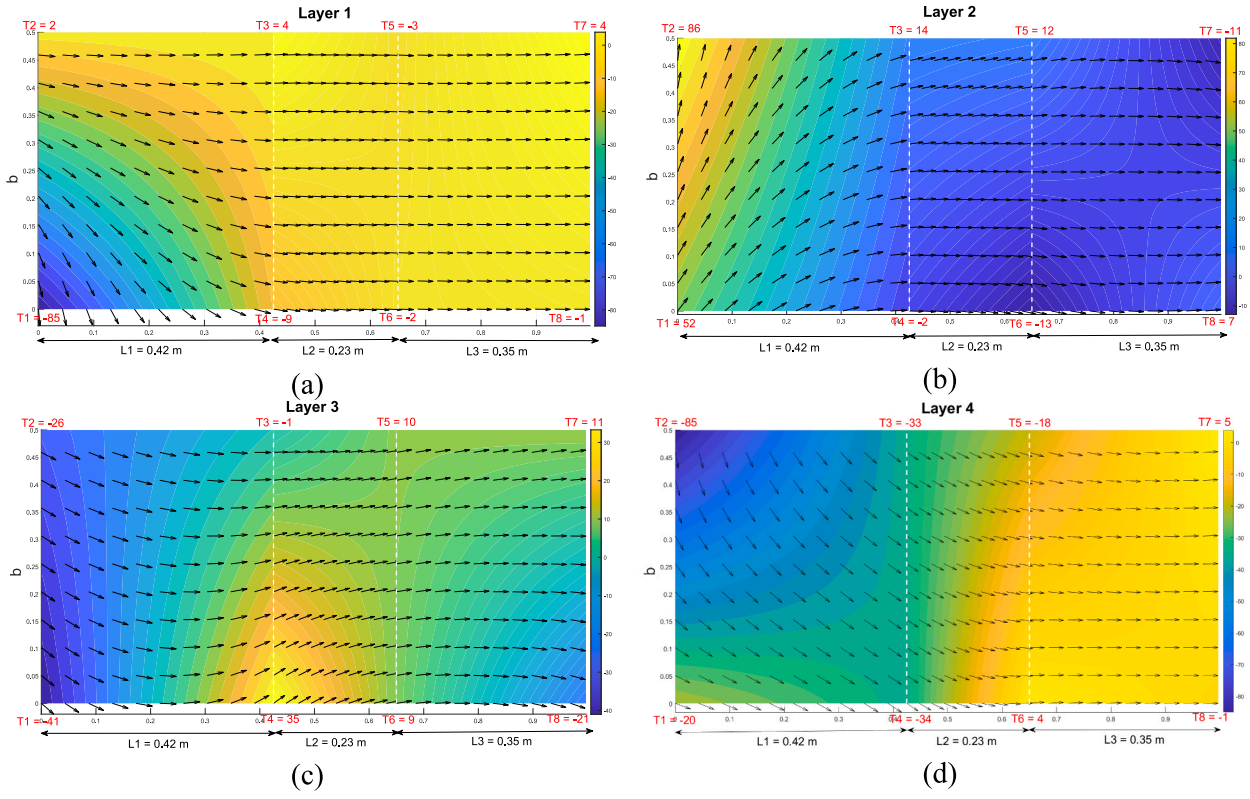

Fig. 14. Layer stacking sequences and designed fiber angles for the panel with CFFF BCs., $R = 5$, and $L/b = 2$. Subfigures (a–d) correspond to Layer 1 through Layer 4, respectively.

outcomes of our study demonstrate a favorable agreement with the findings in existing literature.

3.2. Parametric and optimization studies

Sections 2.2–2.4 present the theoretical and numerical framework used to model and optimize the composite panel. The structure is modeled using FSDT, and the governing equations are solved via the GDQ method, implemented in an *in-house MATLAB code*. This code is coupled with a GA module to perform the optimization.

In this section, the GA is applied to maximize the FNF of composite panels by optimizing the fiber angles for various geometries and boundary conditions. Following the optimization, the nonlinear frequency behavior of the resulting optimum panel is analyzed separately. The stacking sequence for the eight-layered composite cylindrical panel with a CFP is provided in Eqs. (2)–(4). For comparison purposes, a conventional unidirectional (UD) layup sequence is also considered as the reference configuration and given in Eq. (26).

$$\left[\Theta^1/\Theta^2/\Theta^3/\Theta^4\right]_{sym} \rightarrow \left[0^\circ/+45^\circ/-45^\circ/90^\circ\right]_{sym} \tag{26}$$

The geometrical dimensions of the composite cylindrical panel, along with its material properties, are presented in Table 2, using the parameters defined in Fig. 3.

In the present study, a convergence analysis was conducted to ensure the accuracy of the numerical solution using the GDQ method. The results shown in Fig. 7 demonstrate convergence for the selected number of elements in x, y, and z directions, with $n_x = 13$, $n_y = 13$, and $n_z = 3$. The figure presents the GDQ grid convergence study by varying in-plane discretization ($n_x = n_y = 11,12,13,14,15$) and thickness layers ($n_z = 2,3,4$). As observed, the normalized natural frequencies for Mode 1 and Mode 2 stabilize as the mesh is refined, particularly beyond $n_x = n_y = 13$ and $n_z = 3$, where frequency variations become negligible. This trend confirms that the chosen resolution offers a good balance between computational efficiency and accuracy, eliminating the need for further refinement.

Fig. 8 provides a schematic representation of the element distribution along the panel's width and length, clearly illustrating the region boundaries and their distinct characteristics. The figure shows a 3D mesh representation of Multi-Region (M−CFP) and Single-Region (S-CFP) curvilinear fiber path (CFP) panels, illustrating the discretization used in the numerical model. Both configurations are discretized in the x, y, and z directions according to the GDQ-based convergence parameters n_x, n_y and n_z. In M−CFP, the panel surface is divided into three design regions along the x-axis to allow spatial variation in fiber orientation, while S-CFP uses a single region. The symmetric layer stacking through the thickness and structured mesh enable efficient and accurate evaluation of vibrational behavior,

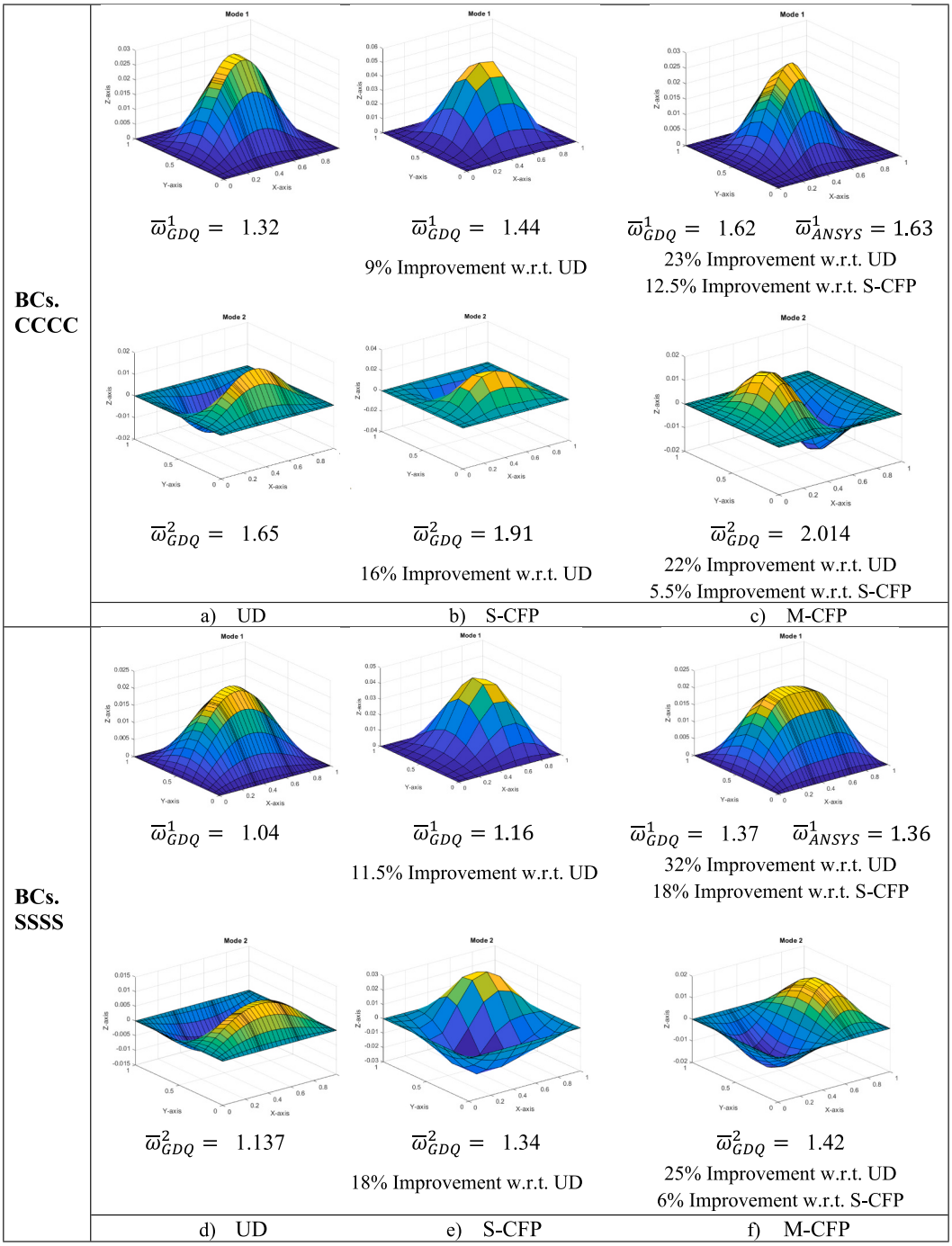

Fig. 15. Comparison of the fundamental natural frequency (FNF) and second mode shapes for panels with CCCC (a–c) and SSSS (d–f) boundary conditions, using three configurations: unidirectional (UD), single-region curvilinear fiber path (S-CFP), and multi-region curvilinear fiber path (M−CFP). Results are shown for a cylindrical panel with $R = 10$ and $L/b = 1$, highlighting performance improvements of S-CFP and M−CFP over the conventional UD design.

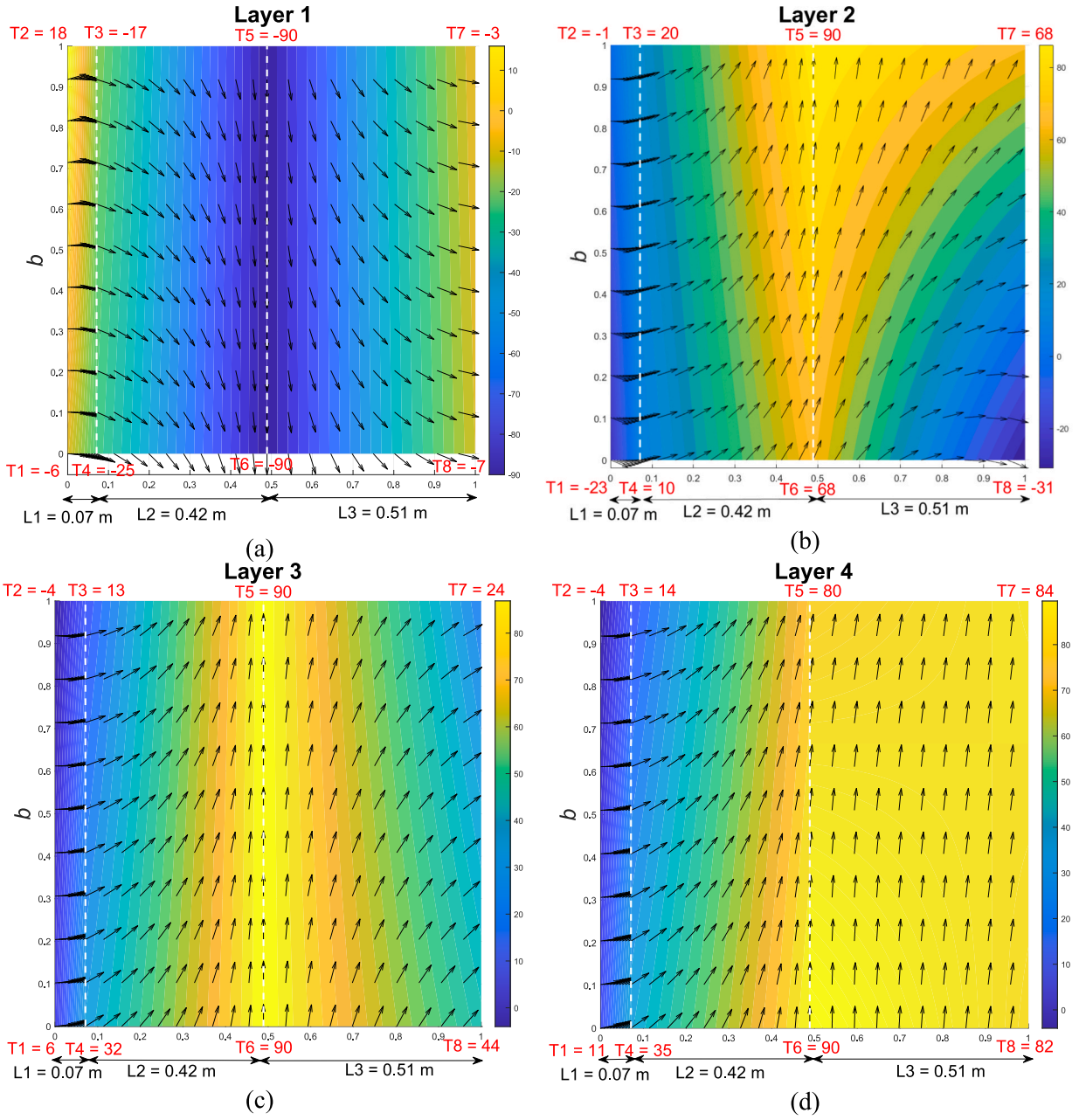

Fig. 16. Layer stacking sequences and designed fiber angles for the panel with CCCC BCs., $R = 10$, and $L/b = 1$. Subfigures (a–d) correspond to Layer 1 through Layer 4, respectively.

highlighting how design zoning and mesh resolution support performance optimization.

To maximize the FNF, the fiber angles defined in Eq. (5) are adjusted, and the corresponding FNF are evaluated to identify the optimal configuration. Due to the symmetric nature of the composite lamination sequence, the optimization process focuses only on the fiber angles of the first four layers. A schematic representation of the panel's geometrical shape is provided in Fig. 9a and b. The non-dimensional FNF utilized in this study is derived from Eq. (27) [4].

$$\overline{\omega}_{FNF} = \frac{1}{2\pi}\omega_{FNF}R\sqrt{\frac{\rho}{E_1}} \tag{27}$$

The GA configuration seen in Table 3 is designed to adapt to different optimization strategies—Global, Local, and Balanced searches—using a flexible and structured approach. For Global Search, the algorithm explores the solution space extensively with 100 generations and a population size of 72, determined as twice the number of optimization parameters. For Local Search, the focus is on

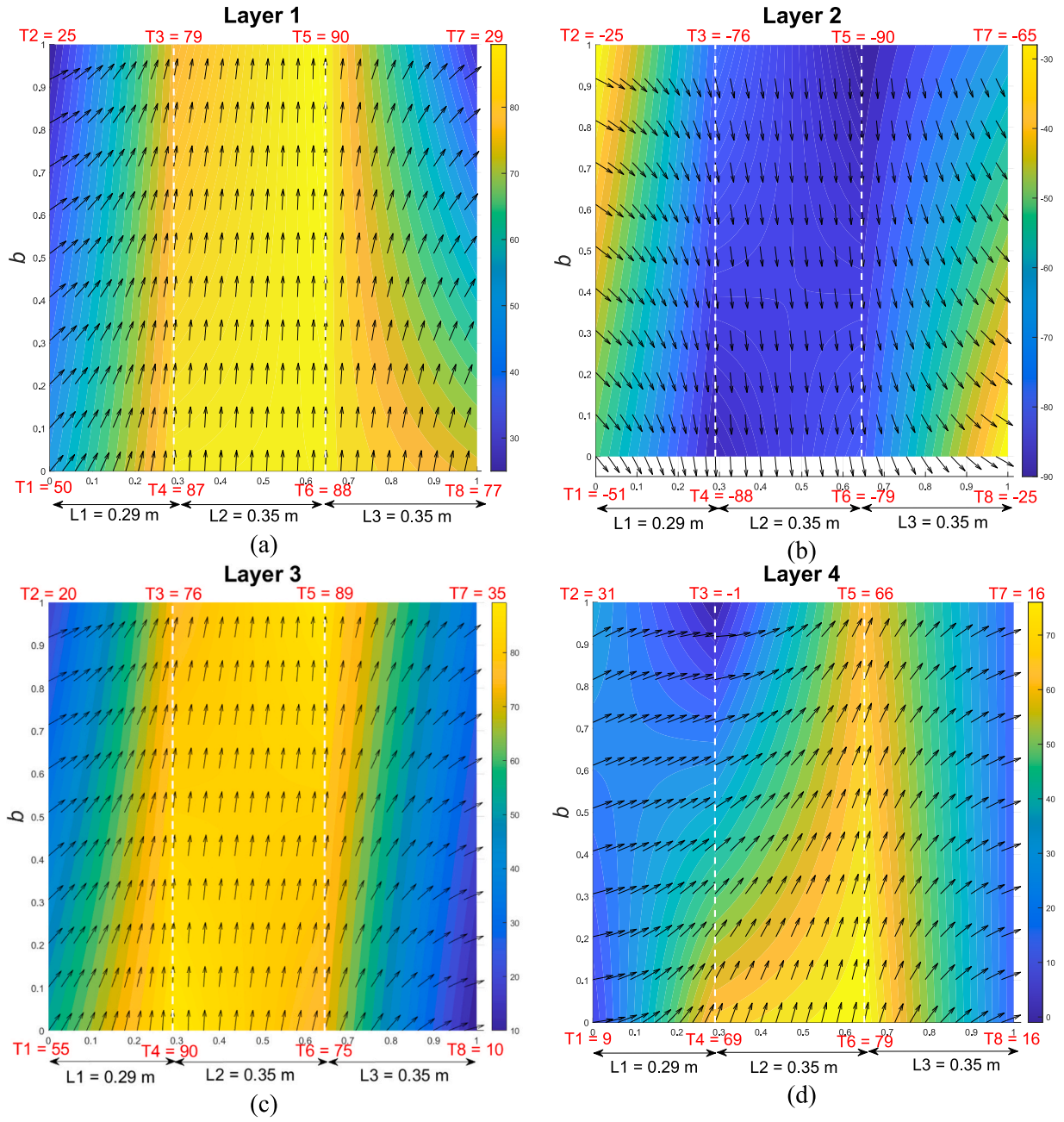

Fig. 17. Layer stacking sequences and designed fiber angles for the panel with SSSS BCs., $R = 10$, and $L/b = 1$. Subfigures (a–d) correspond to Layer 1 through Layer 4, respectively.

fine-tuning solutions within a smaller region, running for up to 50 generations or stopping earlier upon convergence. The Balanced Search, combining elements of both strategies, also runs for 50 generations to achieve a trade-off between exploration and exploitation.

The algorithm employs a Stochastic Selection mechanism with Linear Ranking, ensuring diversity while maintaining a bias toward high-performing solutions. The crossover process utilizes two methods—Uniform and Simulated Binary—each with a 50 % probability, a single crossover point, and a distribution parameter of 2.0 to encourage moderate variability. Mutation is carried out using a Normally Distributed method with a 5 % mutation rate. The standard deviation values for mutation vary across strategies, starting at 0.020 and reducing to 0.001 for Local Search, starting at 0.050 and reducing to 0.010 for Balanced Search, and remaining constant at 0.100 for Global Search. These settings collectively enable the algorithm to balance convergence efficiency with solution diversity across varying optimization scenarios.

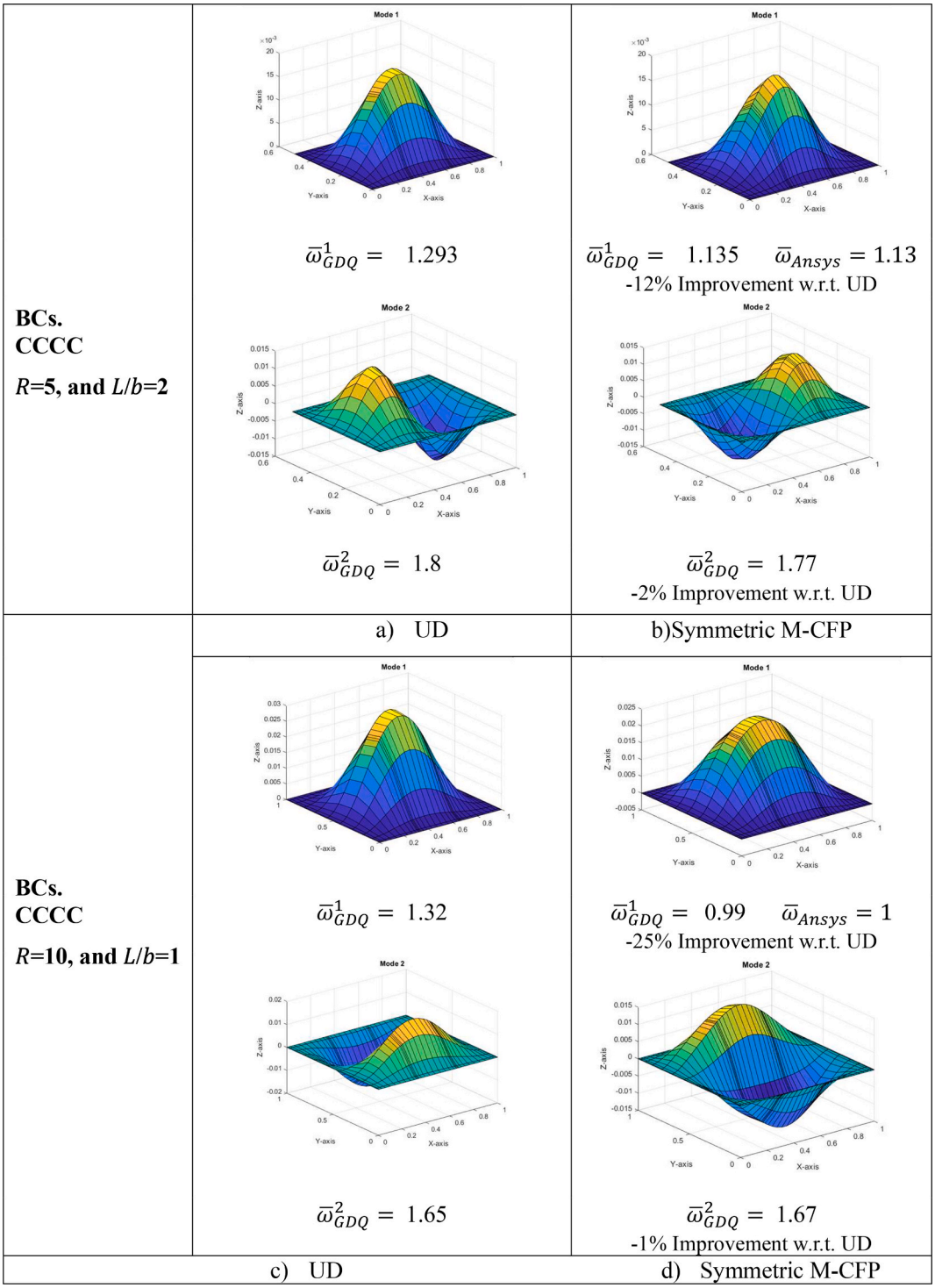

Fig. 18. Comparison of the fundamental natural frequency (FNF) and second mode shapes for panels with (a,b) CCCC BCs. and $R = 5$ and $L/b = 2$ and (c,d) CCCC BCs. and $R = 10$ and $L/b = 1$, using three configurations: unidirectional (UD) and Symmetric multi-region curvilinear fiber path (Symmetric M−CFP).

The results of GA optimizer for the panel with CCCC and CFFF BCs. are depicted in Fig. 10. The GA effectively explores the design space by evaluating thousands of design points to maximize the FNF while adhering to the imposed constraints. Feasible solutions, marked by green circles, represent designs that satisfy all constraints, including geometric and physical limitations like MAC. Infeasible

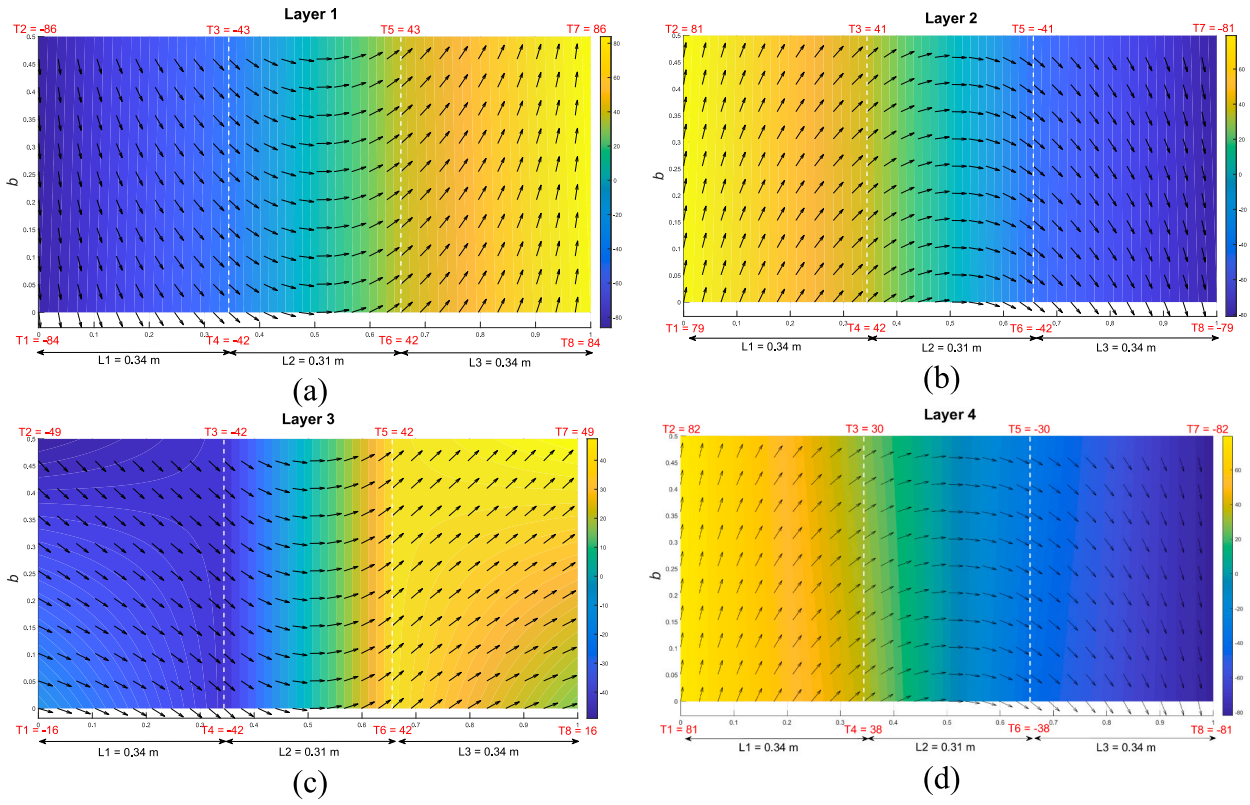

Fig. 19. Layer stacking sequences and designed fiber angles of panel with symmetric stacking sequence layers with CCCC BCs., $R = 5$, and $L/b = 2$. Subfigures (a–d) correspond to Layer 1 through Layer 4, respectively.

solutions, shown by red circles, identify regions where constraints are violated. The gray history line traces the evolution of the FNF for all evaluated designs, while the blue convergence line demonstrates a clear upward trend, reflecting the optimizer's ability to refine designs toward an optimal configuration. Ultimately, the GA achieves convergence at a high FNF, underscoring its robustness and efficiency in solving complex optimization problems for composite panels.

To ensure smooth transitions between regions, adjacent regions should share consistent corner fiber angles at their boundaries, maintaining continuity across the panel. The bilinear interpolation formulation also allows for significant design flexibility, as each region can have unique dimensions and corner angles, enabling detailed customization of fiber paths to optimize structural performance.

Fig. 11 and15 present a comparison of the optimal FNF and the corresponding mode shapes for the CFP and UD panel configurations. The optimization variables, including fiber angles (T_1 to T_8), fiber streams and the CFP functions, are illustrated in Figs. 12-14 and 16-17. The results are derived for cylindrical panel configurations with aspect ratios $L/b = 2$ and $L/b = 1$, radii $R = 5$ and $R = 10$, under fully clamped (CCCC), fully simply supported (SSSS) and one side clamped (CFFF) boundary conditions, along with the maximum associated FNFs. By considering the UD panel as the baseline configuration and S-CFP (Single-Region) configuration, the effectiveness and benefits of the optimization algorithm in M−CFP (Multi-Region) configuration are clearly demonstrated.

Figs. 11-14 present the optimization results for a composite panel with CCCC, SSSS and CFFF BCs., radius of $R = 5$, and an aspect ratio of $L/b = 2$. Fig. 11 analyzes the first two vibration modes—FNF (Mode 1) and the second natural frequency (Mode 2)—of the M−CFP panel and compares the results with those of the UD and S-CFP configurations. The FNF results are compared with those obtained using ANSYS ACP to validate the structural model, solution methodology, and CFP simulation. The comparison confirms the accuracy and reliability of the optimization framework. For the CCCC, SSSS, and CFFF boundary conditions, the M−CFP configuration shows significant improvements in the FNF (Mode 1) of 57 %, 50 %, and 27 %, respectively, compared to the UD configuration. When compared to the S-CFP configuration, the corresponding improvements are 24 %, 26 %, and 17 %, demonstrating the effectiveness of the CFP design. The associated stacking sequence for the M−CFP, the designed fiber angles for the three regions, and the region lengths for all four layers and CCCC, SSSS and CFFF BCs are illustrated in Figs. 12-14, providing a detailed visualization of the optimized configuration for each layer. During the optimization process, the MAC value for this panel configuration is determined as $K_{\max} = 3.18$. This result underscores the potential of the CFP design in enhancing the vibrational performance of composite panels under specified boundary and geometric conditions.

Figs. 15-17 show the optimization results for a composite panel with CCCC and SSSS BCs., $R = 10$, and $L/b = 1$. The FNF results, validated against ANSYS ACP simulations, demonstrate the accuracy of the structural model and M−CFP approach. Fig. 15 shows

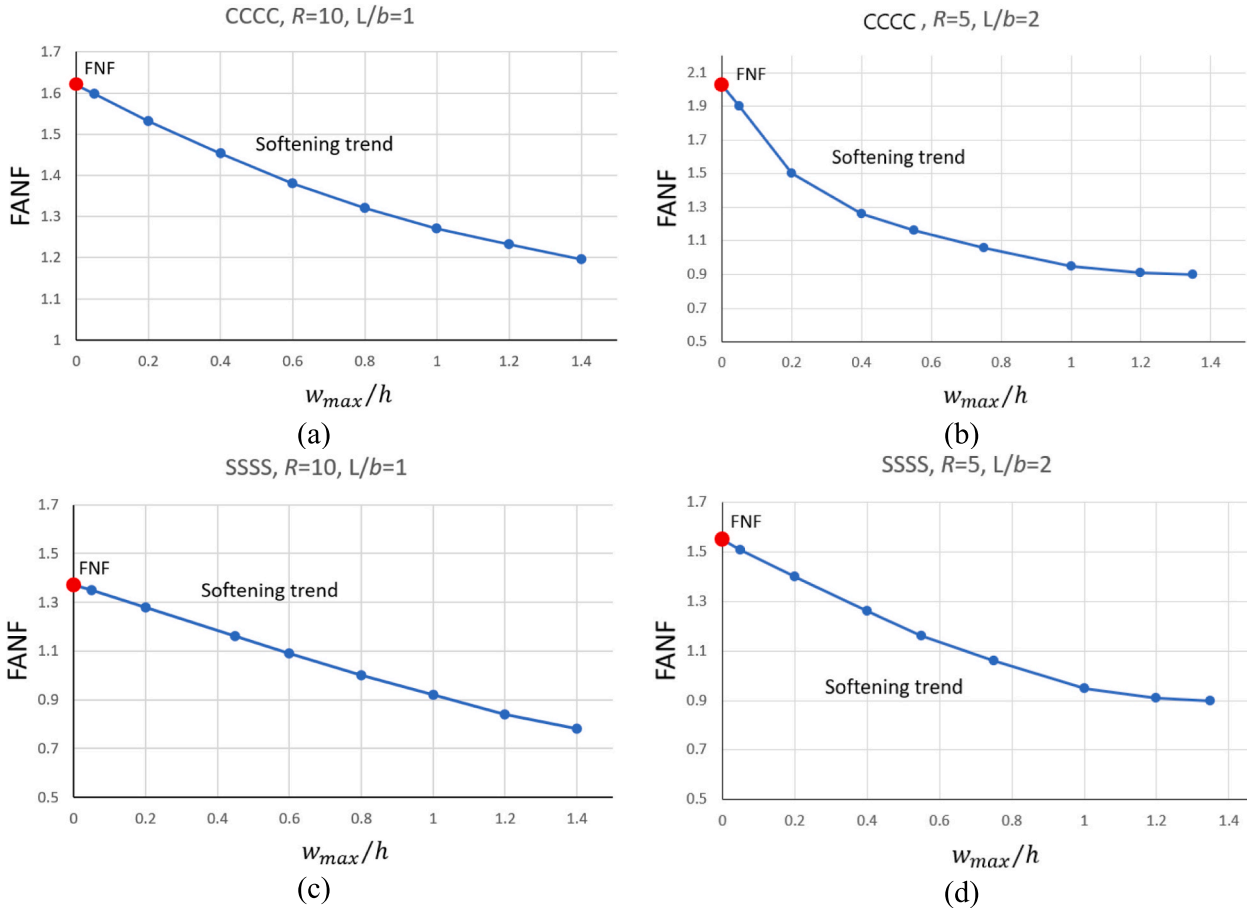

Fig. 20. Nonlinear frequency behavior of the composite panel with the optimum VSCL under (a,b) CCCC and (c,d) SSSS boundary conditions. The plots show the variation of the FANF with increasing normalized transverse displacement w_{max}/h.

improvements of 23 % and 32 % in FNF over the conventional UD configuration, and 12.5 % and 18 % over the S-CFP configuration, demonstrating the enhanced performance and efficiency of the M−CFP design. Figs. 16 and 17 represent the stacking sequence, fiber angle variables, and region lengths across four layers for CCCC and SSSS BCS., respectively. While satisfying the optimization constraints on MAC with $K_{max} = 3.19$, the results demonstrate the CFP design's effectiveness in enhancing the vibrational performance of composite panels.

In the optimization process, an unsymmetrical pattern for the fiber path and design regions in each layer is employed in the simulations. At first glance, as commonly assumed in literature, one might expect that adopting symmetry about the middle lines of the panel would yield a more efficient and aesthetically pleasing fiber stream, leading to enhanced optimization results. However, the findings of this study reveal a different perspective. Despite the panel geometry and boundary conditions being symmetric along one or two axes, the fiber path and design region lengths do not necessarily need to follow symmetry to achieve the maximum FNF. In fact, the highest FNF values are obtained with unsymmetrical CFP patterns in the design regions. Figs. 11, 15, and 18 demonstrate that, for panels with identical configurations, the use of unsymmetric design region patterns—as shown in Figs. 11 and 15—leads to significantly higher improvements in FNF compared to symmetric patterns shown in Fig. 18. Specifically, the unsymmetric configurations achieve enhancements of 57 % and 23 % in FNF relative to the UD configuration, while the symmetric counterparts result in reduced performance, with FNF deteriorations of 12 % and 25 % under CCCC boundary conditions for $R = 5$, $L/b = 2$ and $R = 10$, $L/b = 1$, respectively. This highlights the importance of allowing for unsymmetric designs in optimization studies, as they can better exploit the structural and vibrational characteristics of composite panels under given boundary conditions and geometries. Fig. 19 shows the associated fiber streams and fiber angles for symmetric configuration.

3.2.1. Nonlinear analysis

Fig. 20 offers a representation of the relationship between the FANF and the non-dimensional oscillation amplitude w_{max}/h for the cylindrical panel, where w_{max} represents the maximum oscillation amplitude of the panel in its fundamental vibration mode. The oscillation amplitude w_{max} is applied to the governing system as an initial condition, and the FANF is subsequently determined for each specific initial condition. This demonstrates that the fundamental nonlinear frequency is amplitude-dependent, a behavior that

contrasts significantly with the linear dynamic response, where frequency remains constant regardless of vibration amplitude. To provide a clear perspective, the FNF is also presented, offering insights into the softening and hardening behavior trends observed in the panels under different configurations. The stacking sequence that yields the optimized FNF, as calculated in the previous section for the CFP panels, is utilized as a reference in this analysis. The nonlinear frequency behavior of these optimized panels is thoroughly examined to assess the amplitude-dependent dynamic response. The results aim to highlight the performance achieved through fiber angle optimization and the distinct nonlinear characteristics arising from the selected layup configurations. The amplitude-dependent frequency (FANF) behavior presented in Fig. 20 reveals a consistent softening trend with increasing normalized transverse displacement ($w\max/h$), which is characteristic of geometrically nonlinear vibration in composite structures. To contextualize these findings, the results have been benchmarked against established nonlinear models reported in the literature. Notably, the softening behavior observed in the current study aligns closely with the results of Farsadi et al. [4] and Ribeiro [45] who conducted nonlinear lay-up optimization of variable stiffness composite cylindrical panels and reported similar amplitude-dependent reductions in natural frequencies under free vibration conditions. This agreement supports the validity of the nonlinear modeling framework employed in the present work and highlights the importance of capturing such nonlinear trends when designing high-performance variable stiffness laminates for vibration-sensitive applications.

4. Conclusion

In this study, the influence of fiber angle variation on the free vibration behavior of VSCL cylindrical panels was investigated for two types of boundary conditions (CCCC, SSSS and CFFF) and varying non-uniform geometries. The GDQ method and Hamilton's principle were employed to analyze the fundamental frequencies of cylindrical panels. The GA was applied to optimize the FNF by determining the optimum fiber angle orientation for each layer in an eight-layer VSCL panel. The study demonstrated that fiber path variations, panel geometry (radius ratios $R = 5{,}10$ and aspect ratios $L/b = 2{,}1$), and boundary conditions significantly influence the dynamic characteristics, including natural frequencies (FNF), nonlinear amplitude-dependent frequencies (FANF), and mode shapes. Additionally, the nonlinear frequency behavior of the optimized VSCL panels was examined. The FNF results are evaluated against conventional UD and S-CFP (Single-Region CFP) configurations, demonstrating that the optimized M−CFP panels achieve significantly enhanced performance. Notably, the M−CFP (Multi-Region CFP) designs exhibit higher maximum frequencies and distinct nonlinear behaviors, including softening or hardening trends. These outcomes emphasize the effectiveness of multi-region fiber angle optimization in improving the dynamic response of composite cylindrical panels. The study further highlights the influential roles of boundary conditions, fiber path distribution, and panel geometry in shaping both linear and nonlinear vibrational characteristics, offering a comprehensive framework for the design of high-performance composite structures. Future work will explore the use of gradient-based or hybrid optimization methods, such as the Method of Moving Asymptotes (MMA), to complement the current genetic algorithm approach. Despite challenges in computing gradients due to the problem's nonlinearity, such methods could provide valuable insights into improving convergence and optimization efficiency.

CRediT authorship contribution statement

Touraj Farsadi: Writing – original draft, Validation, Software, Project administration, Investigation, Funding acquisition, Formal analysis, Conceptualization. **Majid Ahmadi:** Validation, Software, Investigation, Funding acquisition, Formal analysis, Conceptualization. **Shakir Jiffri:** Writing – review & editing. **Hamed Haddad Khodaparast:** Writing – review & editing. **Hasan Kurtaran:** Writing – review & editing. **Michael I. Friswell:** Writing – review & editing. **Sebastiano Fichera:** Writing – review & editing.

Declaration of competing interest

The authors declare that they have no known competing financial interests or personal relationships that could have appeared to influence the work reported in this paper.

Acknowledgements

This study has been supported by the Scientific and Technological Research Council of Türkiye (TÜBİTAK, Project No. 220 N396). The authors gratefully acknowledge the support of this study.

Data availability

Data will be made available on request.

References

[1] R. Olmedo, Z. Gurdal, Buckling response of laminates with spatially varying fiber orientations. In 34th Structures, Structural Dynamics and Materials Conference, 1993.
[2] B.F. Tatting, Z. Gürdal, and D, Jegley, Design and manufacture of elastically tailored tow placed plates, 2002.
[3] T. Farsadi, D. Asadi, H. Kurtaran, Fundamental frequency optimization of variable stiffness composite skew plates, Acta Mech. 232 (2) (2021) 555–573.

[4] T. Farsadi, M. Rahmanian, H. Kurtaran, Nonlinear lay-up optimization of variable stiffness composite skew and taper cylindrical panels in free vibration, Compos. Struct. 262 (2021) 113629.
[5] T. Farsadi, Enhancement of static and dynamic performance of composite tapered pretwisted rotating blade with variable stiffness, J. Vib. Acoust. 143 (2) (2021) 021009.
[6] M.X. He, X. Lyu, Y. Zhai, Y. Tang, T. Yang, Q. Ding, Multi-objective optimal design of periodically stiffened panels for vibration control using data-driven optimization method, Mech. Syst. Sig. Process. 160 (2021) 107872.
[7] Z. Meng, G. Yang, Q. Wu, S. Xiao, Q. Li, Reliability-based topology optimization for fundamental frequency maximization with frequency band constraints, Mech. Syst. Sig. Process. 195 (2023) 110295.
[8] Z. Duan, Y. Liu, H. Jin, J. Yan, J. Zhu, Concurrent multi-scale design optimization of fiber-reinforced composite material based on an adaptive normal distribution fiber optimization scheme for minimum structural compliance and additive manufacturing, Comput. Methods Appl. Mech. Eng. 434 (2025) 117596.
[9] A.L.F. da Silva, R.A. Salas, E.C.N. Silva, Topology optimization of fiber reinforced structures considering stress constraint and optimized penalization, Compos. Struct. 316 (2023) 117006.
[10] P. Ribeiro, et al., A review on the mechanical behaviour of curvilinear fibre composite laminated panels, J. Compos. Mater. 48 (22) (2014) 2761–2777.
[11] A. Venkatachari, et al., Assessment of certain higher-order structural models based on global approach for bending analysis of curvilinear composite laminates, Compos. Struct. 118 (2014) 548–559.
[12] H. Akhavan, P. Ribeiro, Reduced-order models for nonlinear flutter of composite laminates with curvilinear fibers, AIAA J. 57 (7) (2019) 3026–3039.
[13] H. Akhavan, P. Ribeiro, Natural modes of vibration of variable stiffness composite laminates with curvilinear fibers, Compos. Struct. 93 (11) (2011) 3040–3047.
[14] J. Fazilati, V. Khalafi, Aeroelastic panel flutter optimization of tow-steered variable stiffness composite laminated plates using isogeometric analysis, J. Reinf. Plast. Compos. 38 (19–20) (2019) 885–895.
[15] D. Asadi, T. Farsadi, A. Kayran, Flutter optimization of a wing–engine system with passive and active control approaches, AIAA J. 59 (4) (2021) 1422–1440.
[16] B. Daraei, S. Shojaee, S. Hamzehei-Javaran, Free vibration analysis of composite laminated beams with curvilinear fibers via refined theories, Mech. Adv. Mater. Struct. 29 (6) (2022) 840–849.
[17] Z. Kheladi, S.M. Hamza-Cherif, M. Ghernaout, Free vibration analysis of variable stiffness laminated composite beams, Mech. Adv. Mater. Struct. 28 (18) (2021) 1889–1916.
[18] Y. Yan, et al., Free vibration analysis of variable stiffness composite laminated beams and plates by novel hierarchical differential quadrature finite elements, Compos. Struct. 274 (2021) 114364.
[19] M. Patni, et al., Efficient 3D stress capture of variable-stiffness and sandwich beam structures, AIAA J. 57 (9) (2019) 4042–4056.
[20] R. Vescovini, et al., Efficient post-buckling analysis of variable-stiffness plates using a perturbation approach, Thin-Walled Struct. 143 (2019) 106211.
[21] P. Hao, et al., Isogeometric buckling analysis of composite variable-stiffness panels, Compos. Struct. 165 (2017) 192–208.
[22] R. Vescovini, L. Dozio, A variable-kinematic model for variable stiffness plates: vibration and buckling analysis, Compos. Struct. 142 (2016) 15–26.
[23] J. Andérez González, R. Vescovini, Simplified approach to nonlinear vibration analysis of variable stiffness plates, Journal of Composites Science 7 (1) (2023) 30.
[24] T. Farsadi, D. Asadi, H. Kurtaran, Nonlinear flutter response of a composite plate applying curvilinear fiber paths, Acta Mech. 231 (2) (2020) 715–731.
[25] M. Rahmanian, T. Farsadi, H. Kurtaran, Nonlinear flutter of tapered and skewed cantilevered plates with curvilinear fiber paths, J. Sound Vib. 500 (2021) 116021.
[26] X. Song, C. Wang, S. Wang, Y. Zhang, Vibration evolution of laminated composite conical shell with arbitrary foundation in hygrothermal environment: experimental and theoretical investigation, Mech. Syst. Sig. Process. 200 (2023) 110565.
[27] H. Farokhi, N. Jamia, H. Jalali, J. Taghipour, H.H. Khodaparast, M.I. Friswell, A nonlinear joint model for large-amplitude vibrations of initially curved panels: reduced-order modelling and experimental validation, Mech. Syst. Sig. Process. 211 (2024) 111239.
[28] P.K. Shahabad, M.R. Anamagh, G. Serhat, I. Basdogan, B. Bediz, Advanced lamination parameter interpolation and extrapolation methods for designing manufacturable variable stiffness laminates, Compos. Struct. 326 (2023) 117608.
[29] G. Serhat, I. Basdogan, Lamination parameter interpolation method for design of manufacturable variable-stiffness composite panels, AIAA J. 57 (7) (2019) 3052–3065.
[30] S. Nozawa, G. Serhat, Topology and fiber path optimization of composite structures: a critical review, Mater. Des. 113699 (2025).
[31] E. Ameri, M.M. Aghdam, M. Shakeri, Global optimization of laminated cylindrical panels based on fundamental natural frequency, Compos. Struct. 94 (9) (2012) 2697–2705.
[32] S. Lee, M.K. Oh, C. Kim, M. Jung, J. Yoo, Multi-scale design of composite material structures for maximizing fundamental natural frequency, Comput. Methods Appl. Mech. Eng. 425 (2024) 116928.
[33] J.X. Shi, T. Nagano, M. Shimoda, Fundamental frequency maximization of orthotropic shells using a free-form optimization method, Compos. Struct. 170 (2017) 135–145.
[34] Z.R. Wani, M. Tantray, E.N. Farsangi, N. Nikitas, M. Noori, B. Samali, T.Y. Yang, A critical review on control strategies for structural vibration control, Annu. Rev. Control. 54 (2022) 103–124.
[35] Z. Gurdal, R. Olmedo, In-plane response of laminates with spatially varying fiber orientations-variable stiffness concept, AIAA J. 31 (4) (1993) 751–758.
[36] Z. Gürdal, B.F. Tatting, C.K. Wu, Variable stiffness composite panels: effects of stiffness variation on the in-plane and buckling response, Compos. A Appl. Sci. Manuf. 39 (5) (2008) 911–922.
[37] H. Wang, J. Chen, Z. Fan, J. Xiao, X. Wang, Experimental investigation on the influence of fiber path curvature on the mechanical properties of composites, Materials 14 (10) (2021) 2602.
[38] G. Rousseau, R. Wehbe, J. Halbritter, R. Harik, Automated fiber placement path planning: a state-of-the-art review, Comput.-Aided Des. Applic. 16 (2) (2019) 172–203.
[39] C. Waldhart, Z. Gurdal, C. Ribbens, August). analysis of tow placed, parallel fiber, variable stiffness laminates. In 37th Structure, Structural Dynamics and Materials Conference, 1996.
[40] A.K. Kaw, Mechanics of composite materials, CRC Press, 2005.
[41] T. Farsadi, M.O. Bozkurt, D. Coker, A. Kayran, Improvement of structural characteristics of composite thin-walled beams using variable stiffness concept via curvilinear fiber placement, Proceedings of the Institution of Mechanical Engineers, Part g: Journal of Aerospace Engineering 235 (14) (2021) 2017–2032.
[42] H. Kurtaran, Geometrically nonlinear transient analysis of moderately thick laminated composite shallow shells with generalized differential quadrature method, Compos. Struct. 125 (2015) 605–614.
[43] W. Han, M. Petyt, Geometrically nonlinear vibration analysis of thin, rectangular plates using the hierarchical finite element method—I: the fundamental mode of isotropic plates, Comput. Struct. 63 (2) (1997) 295–308.
[45] P. Ribeiro, Non-linear free periodic vibrations of open cylindrical shallow shells, J. Sound Vib. 313 (1–2) (2008) 224–245.